2013-12

Statistical Modeling of Human Liver Incorporating the Variations in Shape, Size, and Material Properties

Yuan-Chiao Lu, Andrew R. Kemper, Scott Gayzik, Costin D. Untaroiu[*]
Virginia Tech-Wake Forest University, Center for Injury Biomechanics

Philippe Beillas
Université de Lyon, IFSTTAR

ABSTRACT – The liver is one of the most frequently injured abdominal organs during motor vehicle crashes. Realistic numerical assessments of liver injury risk for the entire occupant population require incorporating inter-subject variations into numerical models. The main objective of this study was to quantify the shape variations of human liver in a seated posture and the statistical distributions of its material properties. Statistical shape analysis was applied to construct shape models of the livers of 15 adult human subjects, recorded in a typical seated (occupant) posture. The principal component analysis was then utilized to obtain the modes of variation, the mean model, and 95% statistical boundary shape models. In addition, a total of 52 tensile tests were performed on the parenchyma of three fresh human livers at four loading rates (0.01, 0.1, 1, and 10 s^{-1}) to characterize the rate-dependent and failure properties of the human liver. A FE-based optimization approach was employed to identify the material parameters of an Ogden material model for each specimen. The mean material parameters were then determined for each loading rate from the characteristic averages of the stress-strain curves, and a stochastic optimization approach was utilized to determine the standard deviations of the material parameters. Results showed that the first five modes of the human liver shape models account for more than 60% of the overall anatomical variations. The distributions of the material parameters combined with the mean and statistical boundary shape models could be used to develop probabilistic finite element (FE) models, which may help to better understand the variability in biomechanical responses and injuries to the abdominal organs under impact loading.

KEYWORDS – statistical shape analysis, soft tissue modeling, liver parenchyma, material properties, constitutive models, strain-rate dependency.

INTRODUCTION

Abdominal injuries caused by motor vehicle collisions have severe consequences (Arajarvi et al., 1987; Cheynel et al., 2011; Greingor and Lazarus, 2006). While the liver, which is the largest abdominal organ, is located in a relatively protected location, it is one of the most frequently injured abdominal organs in frontal vehicle crashes (Elhagediab and Rouhana, 1998). Liver injuries associated with blunt trauma have the highest morbidity and mortality rates of the abdominal injuries (Nahum and Melvin, 2002). Capsule laceration and parenchyma damage are common liver injuries and could be severe (Oniscu et

al., 2006).

A better understanding of the mechanisms of blunt liver trauma during the traffic accidents may help safety engineers optimize the restraint systems in order to reduce the occurrence of liver injuries. Several injury mechanisms of blunt liver trauma, such as crush, deceleration, and acceleration mechanisms (Jin et al., 2013), have been proposed in the medical literature based on the cause of injury, assumed direction and site of the blunt force, and medical images of the injured subjects (Ahmed and Beckingham, 2007; Howes et al., 2012; Jin et al., 2013). While valuable for the management of major blunt liver injuries by emergency surgeons, these injury mechanisms should be validated by experimental and/or computational tests. Recently, high-speed biplane x-ray was used to investigate relative kinematics of the thoraco-abdominal organs

---

Address correspondence to Costin D. Untaroiu[*], Virginia Tech, Center for Injury Biomechanics, VCOM II Building, 2280 Kraft Drive, Blacksburg, VA 24060. Phone: 540-231-8997, Electronic mail: costin@vt.edu

in response to blunt loading (Howes et al., 2012). However, the simplified loading conditions and limited field of view in the x-ray images during impacts makes a complete understanding of injury mechanisms challenging. With the rapid increase in computational power, a higher use of numerical models for vehicle safety research is observed. The human finite element (FE) models are currently the most sophisticated human numerical models, due to their ability to calculate detailed stress/strain distributions inside the model that consequently could be correlated with the risk of injury (DeWit and Cronin, 2012; Li et al., 2010; Mao et al., 2013; Shin and Untaroiu, 2013; Shin et al., 2012; Vavalle et al., 2013). However, the majority of current human models were developed based on the anthropometry of a 50th male and have assigned material models which lack biofidelity (e.g. strain-rate independent). Therefore, to better understand the injuries observed in the field we believed that new modeling approaches are necessary to take into account the variability of subjects in terms of anthropometries and material properties.

Biological systems, such as abdominal organs, contain inherent variability in geometry, and material properties. The combined effects of these differences along with the uncertainty associated with the loading conditions in the input variables could dramatically affect the system response. Probabilistic analyses consider the uncertainties of the input variables (Dar et al., 2002), so each variable is typically represented as a distribution, and a distribution of performance is predicted as output. In contrast, particular values are chosen for each input variable in deterministic studies, and the outputs are provided as certain numerical values, which cannot provide information about the effect of system uncertainties. Probabilistic analyses are widely used in many areas, such as aeronautical (Melis et al., 1999; Palmberg et al., 1987), automotive (Zhang and Liu, 2002), orthopedic studies (Bah and Browne, 2004; Browne et al., 1999; Dar et al., 2002; Mehrez et al., 2005; Ng and Teo, 2004; Nicolella et al., 2001; Nicolella et al., 2006). However, due to high computational cost, simplified FE models (Browne et al., 1999) or idealized cylindrical geometry (Nicolella et al., 2001) are commonly used in these studies. A probabilistic analysis to predict the maximum stress distribution on a cantilever beam FE model, representing an orthopedic cervical fixation plate was reported (Dar et al., 2002). The authors mentioned that this probabilistic method was not very efficient, requiring about 1,000 simulations to get a reasonably smooth distribution; therefore, a simplified FE model was employed. A 3-dimensional (3D) femur-implant

model, in which variability of material properties and loading conditions were considered in order to predict a probability of failure, was also developed (Nicolella et al., 2001). A simplified FE model for this femur-implant structure was used to avoid large computational time, and no geometry variability was considered. To perform complex probabilistic analyses on human liver models in the future, both variations in geometry and material properties of liver parenchyma properties need to be investigated.

Statistical shape models of the abdominal organs represent useful tools for the investigation of the organ variations for medical treatments (Okada et al., 2007; Reyes et al., 2010), and could also be applied to the development of computational statistical models (Lu and Untaroiu, 2013b; Untaroiu et al., 2012). While the shape variations of the abdominal organs (e.g. liver, spleen and kidney) have been investigated in several studies, none of these studies investigated the shape of these organs in an occupant posture or proposed 3D statistical boundary models (Lu and Untaroiu, 2013b).

The statistical shape analysis (SSA) is a common technique to evaluate the size and shape variations. Traditionally, the SSA begins with manual identification of anatomical landmarks on the training shapes, and follows with the model registration which removes translation, rotation, and/or scaling differences (Dryden and Mardia, 1998; Fink and Zelditch, 1997). While some specific landmarks are defined in atlas-based segmentation schemes (Bhatia et al., 2004; Lamecker et al., 2006), the manual land-marking process is time-consuming and it is challenging when few homologous, well-defined anatomical features, are available in complex 2D and 3D shapes (Brett and Taylor, 2000; Davies, 2002; Davies et al., 2010; Fleute et al., 1999; Hufnagel et al., 2009; Marai et al., 2007; Rajamani et al., 2007). Therefore, semi-landmark approaches have been employed in the recent SSA studies. The semi-landmarks are the surface points utilized for the shape reconstruction of the object which are not required to be anatomic feature points (Heimann and Meinzer, 2009). In most semi-landmark approaches, the model registration, automatic landmark identification through correspondence process, and the principal component analysis (PCA) are included as major steps of the construction of 3D statistical shape models. The principal directions of variation, also called "modes of variation", could be represented by eigenvectors calculated from PCA (van de Giessen et al., 2010). Several studies had applied SSA on human internal organs (Chen and Shapiro, 2009; Chen et al., 2010; Davies et al., 2010;

Lamecker et al., 2002; Okada et al., 2007; Reyes et al., 2010), bones (Barratt et al., 2008; Bredbenner et al., 2010; Fripp et al., 2005; Lorenz and Krahnstover, 1999; van de Giessen et al., 2010), and the entire human body (Azouz et al., 2006; Xi et al., 2007). Distal femur and proximal tibia statistical models were also developed to investigate the shape variability of the knee joint (Bredbenner et al., 2010; Fripp et al., 2005). SSA was applied on wrist bones and it was found that the first five modes have the highest variations (van de Giessen et al., 2010). 3D lumbar vertebrae shape models were developed and then the corresponding FE mesh models were built (Lorenz and Krahnstover, 1999). Statistical shape models for human soft tissues such as pancreas (Reyes et al., 2010), liver (Lamecker et al., 2002), kidney and spleen (Chen and Shapiro, 2009; Chen et al., 2010) have also been investigated. All of these recent studies utilized PCA to construct statistical shape models and present at least first three shape modes.

The statistical shapes of the abdominal organs (liver, spleen, and kidney) were investigated in several studies using various approaches. The 3D shape models of human liver, spleen, and right and left kidneys using minimum description length (MDL) for the landmark correspondence were previously reported (Chen and Shapiro, 2009). The shape models of the first three modes of rat kidney using the MDL approach were also constructed (Davies et al., 2010). However, this method involves an extensive optimization process, resulting in substantial computational time (Dalal et al., 2007). The shape models of human livers were reported in a published study (Lamecker et al., 2002). While the first three principal modes of variations were presented, the percent contribution of each principal component (mode) and the examinations of the mode normality were not reported. The shape models of human liver, spleen, and kidney using a multi-level shape model approach (Okada et al., 2007), which divided the organs into anatomical parts, were also reported (Reyes et al., 2010). Since the normalization of the organs was executed, the size differences were not considered in their study. In all of these shape analysis studies, the abdominal organs of the subjects were scanned in supine posture, or the postures used during image data collection were not clearly stated.

Since abdominal organs are soft tissues, their shapes may change in different postures (Beillas et al., 2009; Hayes et al., 2013a). The effects of posture (supine, standing, seated and forward-flexed) on the positions and shapes of the abdominal organs were quantified (Beillas et al., 2009). It was shown that organ volumes were mostly unaffected by postures, but the position of abdominal organs in the supine posture changed up to 40 mm when comparing with the other three postures. Changes in locations and morphologies of abdominal organs between supine and seated postures were also reported (Hayes et al., 2013a). When comparing the seated posture to the supine posture, liver expanded 7.8% cranially and compressed 3.4% and 5.2% in the anterior-posterior and medial-lateral directions, respectively (Hayes et al., 2013a). Similar results were found for spleen and kidney. In conclusion, all these studies suggested that the shapes of the abdominal organs change in different postures mostly due to gravity.

To automatically build statistical shape models from a training set of shapes, finding point correspondence across images becomes an essential task (Chen et al., 2010). Several correspondence approaches to determine the corresponding landmarks between shapes have been proposed and compared in the literature (Chen and Shapiro, 2009; Dalal et al., 2007; He et al., 2009; Lamecker et al., 2002; Styner et al., 2003; van de Giessen et al., 2010). A correspondence approach, which establish landmarks on a selected shape (template), and use the shortest distance between the landmarks on the template surface and the points on the target surfaces to determine the corresponding landmarks on the target surfaces, has been recently proposed (Dalal et al., 2007). However, estimating corresponding points based merely on minimum Euclidean distance was found to be inaccurate in regions with large curvatures (Heimann and Meinzer, 2009), and if the two aligned shapes do not have a certain amount of overlapping, the approach based on shortest distance may fail to establish the correct correspondence (He et al., 2009; He et al., 2010). To solve this problem, an improved correspondence algorithm was proposed using both coordinates and surface normal (Brett and Taylor, 2000; He et al., 2009; van de Giessen et al., 2009). Comparing to each landmark on the template surface, the surface point of a target model with the smallest Euclidean distance and smallest differences between surface normals was chosen as the target landmark. In addition, the iterative thin-plate spline (TPS) algorithm (Bookstein, 1989) could efficiently refine the correspondence and showed (He et al., 2009) a faster performance than the landmark sliding approach proposed previously (Dalal et al., 2007), without loss of accuracy. The current study will therefore adopt the correspondence approach and iterative TPS algorithm (He et al., 2009)

Biomechanical properties of liver parenchyma have been reported from unconfined compression tests

performed on animal tissues (Pervin et al., 2011; Roan and Vemaganti, 2007; Rosen et al., 2008; Tamura et al., 2002; Umale et al., 2013) and human tissues (Kemper et al., 2013; Rosen et al., 2008). Numerous tensile studies have been performed at low level strains on specimens of liver parenchyma for surgical robot control systems and surgeon training systems based on the virtual reality techniques (Chui et al., 2007; Gao and Desai, 2010; Gao et al., 2010; Yeh et al., 2002). Several studies have also investigated the failure properties of liver parenchyma in uniaxial tension (Brunon et al., 2010; Kemper et al., 2010; Santago et al., 2009a; Santago et al., 2009b; Uehara, 1995; Yamada, 1970). An average stress-strain curve and failure data obtained on rabbit livers have been reported (Yamada, 1970), but no loading rate information is provided. The failure data recorded on porcine specimens at four different strain rates have also been reported (Uehara, 1995). To characterize the tissue viscoelasticity under a large frequency range, oscillatory shear tests (Klatt et al., 2010; Liu and Bilston, 2000; Nicolle et al., 2010; Valtorta and Mazza, 2005), impact hammer tests (Umut Ozcan et al., 2011), and indentation tests (Lu and Untaroiu, 2013a; Ottensmeyer, 2001; Samur et al., 2007) have been performed on liver tissues as well. Recently, an extensive study presented the results of a total of 51 tension tests performed on human liver parenchyma at four loading rates (Kemper et al., 2010). The stress-strain curves until failure were obtained using optical markers placed on the specimens. Although these studies provide considerable insight into the factors that affect the tensile response of liver parenchyma, usually only regional (local) properties (e.g. based on optical marker displacements) have been reported. In addition, an implementation of test data of human liver parenchyma into a FE material model is lacking.

The material characterization of bovine liver parenchyma under tensile loading was recently investigated (Untaroiu and Lu, 2013). In this study, it was demonstrated that the properties obtained from the video data analysis (optical marker tracking) do not always accurately represent the force response of the whole samples under tensile loading probably due to tissue inhomogeneity (Gao and Desai, 2010) and/or measurement errors. Therefore, in addition to a marker-based model, a FE-based model was employed in this study as well.

The effects of preservation on the responses of animal livers under different types of loading schemes have been investigated by several studies. Tensile quasi-static tests on parenchyma and capsule samples of porcine livers until failure were conducted

(Brunon et al., 2010) to characterize capsule failure and it was found that freezing preservation significantly affected porcine capsule failure properties. Impact experiments were conducted on bovine livers (Ocal et al., 2010) to investigate the effect of preservation period (1h-48h after harvesting) on its viscoelastic material properties, and it was found that the liver tissue became stiffer and more viscous as it spent more time in the refrigeration preservation at 4°C. The failure stress and the failure strain between fresh and 26-day frozen preserved tissues under uniaxial tensile loading were compared, and significant changes in failure strain were reported (Santago et al., 2009a). Refrigeration storage was also shown to change the porcine liver stiffness in indentation tests (Lu and Untaroiu, 2013a). Therefore, to avoid possible degradation of the tissues after post mortem, the human livers were all tested under fresh conditions in this study.

One previous study (Santago et al., 2009b) found no statistically significant changes in failure tensile stress or strain between liver specimens tested at normal room temperature (24°C) and body temperature (37°C). Therefore, in the current study, the human liver specimens were tested at a temperature close to a normal room temperature (24°C) and within 48 hours of death to minimize the effects of tissue degradation.

The objective of this study was to characterize statistically the shape and material properties of human liver that may help in the development of probabilistic models. Three-dimensional mean and statistical boundary shape models corresponding to human livers in a seated posture were developed. In addition, a specimen-specific FE optimization approach, similar to that used in recent studies (Gras et al., 2012; Hu et al., 2009; Hu et al., 2011; Untaroiu, 2010; Untaroiu et al., 2005), was employed to identify material parameters of liver parenchyma. The average stress-strain curves and failure data were then used to determine the mean and standard deviation of material parameters through a stochastic optimization process. These material and shape models could be later implemented in the probabilistic human FE models.

METHODS

Image Acquisition of Human Liver Shapes

The shapes of human livers used to build the statistical size and shape models were reconstructed from the MRI images of 15 subjects in seated

posture. The demographic data of these subjects included in "Lyon" dataset (Beillas et al., 2009; Lafon et al., 2010) and Wake" dataset (Hayes et al., 2013a; Hayes et al., 2013b) are listed in Table 1. Since the subjects in the two data sets were both scanned at seated posture with slightly different seat angle (<2°), it is acceptable to combine both datasets in the development of statistical shape models of the human liver.

In the "Lyon" dataset, the subjects were seated in a custom built seat, with a seat back angle of 25 degrees to the vertical and a seat pan angle of 9 degrees to the horizontal plane. The height of the seat was adjustable. The MRI scans were performed along the sagittal plane of the subjects. The MRI slice resolution was 256 by 256 pixels, which created an image area of a 400 mm by 400 mm per slice. For each subject, 54 to 60 slices were obtained with a slice thickness of 5mm, and the number of slices was depending on the width of the subject. The subjects were instructed to breathe quietly during the MRI scanning process. The 3D polygonal surfaces were reconstructed from the MRI scans using a custom registration toolbox based on Imod (University of Colorado, Boulder, CO) and Scilab (www.scilab.org) open-source software packages (Lafon et al., 2010).

In the "Wake" dataset, the pixel size of the MRI images was 2.1 mm, and the field of view was 430 mm. The distance between two image slices ranged from 1.5 to 2 mm. The back seat had an angle of 67 degrees to the horizontal plane, and the seat pan was perpendicular to the back seat. The 3D polygonal surfaces were created from the MRI images using Mimics (Materialise, Leuven, Belgium), and were refined using Geomagic Studio (v. 11, Geomagic, Raleigh,NC) software. While there was a slight discrepancy of the back seat angles between these two datasets, it has been shown that the organ volumes and their positions were mostly unaffected between seated and standing postures (Beillas et al., 2009). In both datasets, the resolution of the MRI images used for organ segmentation preserved the shapes of the organs as compared to the raw MRI images (Beillas et al., 2009; Hayes et al., 2013a). Point clouds of approximated 45,000 points for each liver were generated from the polygonal surfaces and used for the following shape analysis.

Table 1. Demographic data of subjects.

Subject ID	Sex	Height (m)	Weight (kg)	Age (years)	Source
F01	Female	1.74	68	41	Lyon
F02	Female	1.72	64	42	Lyon
F03	Female	1.62	53	34	Lyon
F04	Female	1.50	48	24	Wake
F05	Female	1.62	60.8	31	Wake
F06	Female	1.67	91.7	33	Wake
M01	Male	1.75	70	29	Lyon
M02	Male	1.91	88	32	Lyon
M03	Male	1.75	64	29	Lyon
M04	Male	1.69	60	26	Lyon
M05	Male	1.81	80	26	Lyon
M06	Male	1.83	82	37	Lyon
M07	Male	1.60	56.2	27	Wake
M08	Male	1.75	78.6	26	Wake
M09	Male	1.90	102.1	26	Wake

Registration of Shapes

During the registration process, position and orientation differences between livers are minimized such that the only remaining differences between the organs are quantified by size and shape variations. The liver shape from the subject whose height and weight were most close to the 50 percentile adult male (height: 1.76 m; weight: 78.4 kg) was selected as the "template", and the remaining 14 target organ models were registered to it.

The Iterated Closest Point (ICP) method (Besl and McKay, 1992; Zhang, 1992) has become the most common approach for aligning 3D geometrical models due to its simplicity and performance (Brett and Taylor, 2000; Fitzgibbon, 2003; van de Giessen et al., 2010; Zheng et al., 2009). ICP starts with two meshes and an initial guess for their relative rigid-body transform, and then iteratively refines the transformation by repeatedly generating pairs of corresponding points on the meshes and by minimizing an error metric. While the algorithm converges relatively quickly, the initial estimate is not usually good (Fitzgibbon, 2003). Therefore, a modified ICP method, called "LM (Levenberg-Marquardt) -ICP registration" (Fitzgibbon, 2003) was implemented in the current study. The LM-ICP abandons one of the basic characteristics of ICP, its closed-form inner loop, and employs instead a standard iterative non-linear optimizer, called the LM algorithm (Fitzgibbon, 2003). It has been shown that this approach incurs no significant loss of speed (Fitzgibbon, 2003), but allows the extension of ICP to use truly robust statistics, with a concomitant reduction of dependence on the initial estimate.

Correspondence of Landmarks

After the registration, the correspondence process is performed to identify the landmarks on livers, which

could be used for subsequent PCA. Three phases are involved: 1) establishment of the landmarks on the template surfaces; 2) establishment of surface normals for the landmarks on the template surface and the points on target surfaces; 3) establishment of the landmarks on the target surfaces.

The landmarks on the template surface were first constructed by the equal-size cubic grid method (Dalal et al., 2007). This approach assumes that the template surface point is sufficiently dense to represent the surface of the organs, but sufficiently sparse for the construction of a compact statistical shape model. The 3D space for the template surface was divided into equal-size cubic grid cells (Dalal et al., 2007). For each cell containing some surface points, the one closest to the center of this cell was picked as a landmark. The size of the grid cell could be altered to control the number or the density of the template landmarks, and it was chosen as $7 \times 7 \times 7$ mm. The number of the template landmarks was around 1,900, which was close to the number of template landmarks (1,500) of the liver in a multilevel statistical shape analysis study reported previously (Okada et al., 2007).

The second phase was to find the surface normal of each landmark on the template surfaces and of each point on the target surfaces.

The sets of the template landmarks and all target surface points are U_L, and V, respectiveley. Each landmark in U_L is denoted as $u_i \in U_L$, and each point in V is denoted as $v_j \in V$. The following five steps should be achieved to determine the surface normals (Dalal et al., 2007).

Step 1. Find ξ nearest neighbors of u_i or v_j.

Step 2. Construct a 3×3 covariance matrix of nearest neighbors with respect to their x, y, z coordinate positions.

Step 3. Perform Eigen-decomposition of the covariance matrix.

Step 4. The eigenvector corresponding to the smallest eigenvalue is the direction around which least variation is observed. Since we find a small set of ξ-nearest neighbors which should be fairly flat, this smallest eigenvector, denoted as $\overrightarrow{n_i}$ or $\overrightarrow{n_j}$, corresponds to the normal direction of the surface at u_i or v_j. Normalize the eigenvector corresponding to the normal direction.

Step 5. Each surface normal should then be determined whether it points out of surface or points into the surface. A set of dense point clouds is created inside of surfaces. For each u_i (or v_j), a closest point, u_p (or v_p), inside the surfaces is chosen. To position all normals consistently towards outside of the surface, they need to satisfy the equation:

$$\overrightarrow{n_i} \cdot (u_p - u_i) < 0 \text{ and } \overrightarrow{n_j} \cdot (v_p - v_j) < 0 \quad (1)$$

If a surface normal on the template surface has a value of $\overrightarrow{n_i} \cdot (v_p - u_i)$ greater than zero, then a negative sign is given to the surface normal to make its direction towards outside of the surface.

After establishing the surface normals of u_i and v_j, the landmarks on the target surface were found in the third phase using a correspondence approach (He et al., 2009). The following three steps were achieved to find the target landmarks.

Step 1. For each $v_j \in V$, find its closest landmark $u_i \in U_L$ based on the Euclidean distance. Several v_j may select the same u_i as their closest landmark on U_L.

Step 2. For each $u_i \in U_L$, group the set of $v_j \in V$ that select this u_i as their closest landmark on U_L and denote this set as V_i.

Step 3. If there is only one point in V_i, this point is chosen as the corresponding landmark of u_i on the target surface. Move this point to the set of the target landmark V_L and remove the point from V. If there are more than one point in V_i, select one point from V_i whose surface normal is closest to the surface normal of u_i. Move this point to the set of the target landmark V_L and remove the point from V. If there is no points in V_i, select one closest point from V based on the Euclidean distance and assign this point as the corresponding landmark of $u_i \in U_L$. Move this point to the set of the target landmark V_L and remove the point from V. The resulting set of $v_i \in V_L$ are the corresponding landmarks on the target surface.

Refining the Target Landmarks by Iterative TPS

After the initial corresponding landmarks between template and target surfaces were established, the quality of the target landmarks could be further improved by iterative TPS algorithm through transformation functions (Belongie et al., 2002; Bookstein, 1989; He et al., 2009). A transformation function T_f was calculated based on the initial correspondence between template and target

landmarks, U_L and V_L. The number of landmarks in both U_L and V_L is n_L. The landmarks in U_L and V_L are $u_i = (u_{ix}, u_{iy}, u_{iz})$ and $v_i = (v_{ix}, v_{iy}, v_{iz})$, $i=1,\ldots,n_L$, where u_i and v_i are the corresponding landmarks for the same i. The TPS function which transforms the target landmarks to the template landmarks could be expressed as:

$$f(v_{ix}, v_{iy}, v_{iz}) = a_0 + a_x v_{ix} + a_y v_{iy} + a_z v_{iz} + \sum_{j=1}^{n_L} w_j \phi(\| (v_{jx}, v_{jy}, v_{jz}) - (v_{ix}, v_{iy}, v_{iz}) \|) \quad (2)$$

where $\phi(r)=r$ in 3D case. Therefore, each TPS function has n_L+4 parameters (a_0, a_x, a_y, a_z, $w_1,\ldots,w_{n_L}$). Three TPS functions, f_x, f_y, f_z, are utilized to represent the transformation function T_f of x, y, z coordinates.

$$T_f(v_{ix}, v_{iy}, v_{iz}) = \left(f_x(v_{ix}, v_{iy}, v_{iz}), f_y(v_{ix}, v_{iy}, v_{iz}), f_z(v_{ix}, v_{iy}, v_{iz}) \right) = (u_{ix}, u_{iy}, u_{iz}) \quad (3)$$

Each TPS functions (f_x, f_y, and f_z) has the same form as Eq. 2; therefore, Eq. 3 contains $3n_L$ simultaneous equations with a total of $3(n_L + 4)$ unknown parameters. For each TPS function, four additional constraints are imposed (Belongie et al., 2002):

$$\sum_{i=1}^{n_L} w_i = 0 \text{ and}$$

$$\sum_{i=1}^{n_L} w_i x_i = \sum_{i=1}^{n_L} w_i y_i = \sum_{i=1}^{n_L} w_i z_i = 0 \quad (4)$$

Thus, these $3(n_L+4)$ parameters in each transformation function T_f can be simply solved by the $3(n_L + 4)$ simultaneous equations (Eq. 3 and 4). The transformation function T_f can be applied to the entire set of the target points V.

The initial corresponding landmarks U_L and V_L are first utilized to estimate a transformation function T_f. This transformation function T_f is then used to transform all points in V, and the transformed points are denoted as V^1. The Phase 3 in the Section "Correspondence of Landmarks" is applied to U_L and V^1 to find a new set of landmarks from V^1, denoted as V_L^1. A new transformation function T_f^1 can be estimated by U_L and V_L^1, which transform the points on V^1 to a new set of points, denoted as V^2. Continuing this transformation process with k iterations, the landmark set V_L^k on surface V^k can be determined. The indices of the target landmarks are tracked during each iteration so the k-iteration target landmarks can be mapped to their original positions on V. Five iterations were executed for each

correspondence calculation between two surfaces in this study. A CPU time of about 1.5 hours (on Microsoft Windows workstations equipped with Intel Pentium Dual 3.10GHz processors) was required to obtain good corresponding landmarks between one template and 14 target surfaces using 5-iteration TPS for human livers. The surface points are almost evenly distributed after several TPS iterations without further substantial moving of target landmarks, and the initial correspondence error can be greatly reduced, as demonstrated previously (Belongie et al., 2002; He et al., 2009).

Principal Component Analysis

The mean shape and its deviations were computed using PCA, based on the established landmarks (Bredbenner et al., 2010; Chen et al., 2010; Styner et al., 2003). PCA was used to determine the modes of variation and to define axes that are aligned with the principal directions. Let N be the number of 3D training shapes and P be the number of 3D landmarks per model. Conventionally, each shape can be represented by a vector x_k whose dimension is $3P \times 1$ where k=1,...,N. The mean vector $\bar{x}$ and the covariance matrix Ψ are computed from the set of object vectors as (Styner et al., 2003):

$$\bar{x} = \frac{1}{N} \sum_{k=1}^{N} x_k; \Psi = \frac{1}{N-1} \sum_{k=1}^{N} (x_k - \bar{x}) \cdot (x_k - \bar{x})^T \quad (5)$$

As mentioned by Heimann and Meinzer(Heimann and Meinzer, 2009), an Eigen-decomposition on Ψ delivers max(N-1,3P) principal modes of variation, e_i (eigenvectors), and their respective variances η_i (eigenvalues), where i stands for the ith mode. The sorted eigenvalues η_i and eigenvectors e_i of the covariance matrix Ψ are the principal directions spanning a shape space with $\bar{x}$ at its origin. The modes of variation are orthogonal and thus statistically independent. A mode with a high variance describes a larger part of the total size and shape variation between shapes. The percentage of variability of each mode can therefore be defined as $\eta_i / \sum_{i=1}^{N-1} \eta_i$.

Typically, only the first few modes with large eigenvalues (i.e. large variance) describe meaningful size and shape variations. The modes with smaller eigenvalues mainly describe noise that emanates from scanning and random point sampling. The number of elements in each data vector is larger than the number of shapes and therefore the covariance matrix has as many non-zero eigenvalues as the number of shapes minus one, i.e. N-1 (van de Giessen et al., 2010).

Each mode of variation is a dimension of the distribution space that describes similar shapes to the livers used in this study. Objects $\tilde{x}_j$ in the shape space are described as a linear combination of the eigenvectors on $\bar{x}$ (Eq. 6).

$$\Psi \cdot e_i = \eta_i e_i;$$

$$\tilde{x}_j = \bar{x} + \sum_{i=1}^{q} h_i e_i \qquad (6)$$

where e_i are the eigenvectors (dimension: $3P \times 1$ for each i) of the covariance matrix Ψ (dimension: $3P \times 3P$) that describe a set of orthogonal modes of size and shape variation, h_i are shape parameters that control these modes of variation, and q is the number of preselected modes of variation (Davies, 2002; Fleute et al., 1999). The first few modes of the liver size and shape models, which contributed more than 5% of the overall variation for each mode, as demonstrated in a previous study by investigating the scaphoid bones (van de Giessen et al., 2010), were presented as -3SD (standard deviation), mean, and +3SD for each mode.

Distribution of Shapes

To satisfy the conditions for developing the size and shape models, it is necessary to examine the normality of the principal component scores (van de Giessen et al., 2010). These scores, calculated as linear combinations of the original landmarks and the principal components, are the positions of each abdominal organ in this new coordinate system of principal components. The scores for each mode can be plotted as a histogram, and their distributions could be tested whether they are not significantly different from normal distributions. A series of Kolmogorov–Smirnoff tests (Lilliefors, 1967) on the similarity between standardized principal component scores and a standard normal distribution were conducted to test the null hypothesis that the principal component scores are normally distributed. The distributions of principal component scores with p-values greater than 0.05 were judged to be not significantly different from the normal distribution.

Statistical Boundary Shape Models

The most commonly used Anthropomorphic Test Dummies (ATDs), so called "50th percentile" ATD,

try to approximate median male seated height and body weight. In an effort to cover the variation in size and shape that reflect the whole occupant populations, different percentile ATDs are developed as well (e.g. 5th percentile female and 95th percentile male). The distributions of mass and seated height are usually the only variables used in development of these percentile ATDs (Daruwalla et al., 2010; Untaroiu et al., 2008). However, several studies showed that the mass and stature only describe part of the complexity of the human body's shape and only captures a small percentage of the population (Azouz et al., 2006; Xi et al., 2007). To mitigate that problem, this study utilized a novel approach for developing "statistical boundary shape models" (or simply "boundary models") based on SSA (Lu and Untaroiu, 2013b).

The essential difference between the percentile models and boundary models is how they are created. The percentile models were traditionally developed (by scaling) based on the percentiles of the anthropometric data (e.g. mass and stature). However, the boundary models are developed from the multi-normal distributions of the shape modes which try to cover a percentage of the whole population (Lu and Untaroiu, 2013b).

The mean model is determined as the mean of the corresponding landmarks (Reed et al., 2009), i.e. $\bar{x}$ in Eq. 5, and the PCA is applied to identify the most significant modes of liver size and shape models, which are then utilized to construct the boundary models. While the mean model is unique, the definition of boundary models constructed from principal modes is challenging.

The term "κ% boundary models" (Lu and Untaroiu, 2013b), was used to define the boundary models which cover κ% of overall population. For example, if the distributions of the principal component scores are not significantly different from normal distribution (see Section "Distribution of Shapes"), the shape space [-1.96 SD, 1.96 SD](Untaroiu et al., 2013) of each mode will cover 95% of the overall population (Fig. 1, Boundary Models (Lu and Untaroiu, 2013b)).
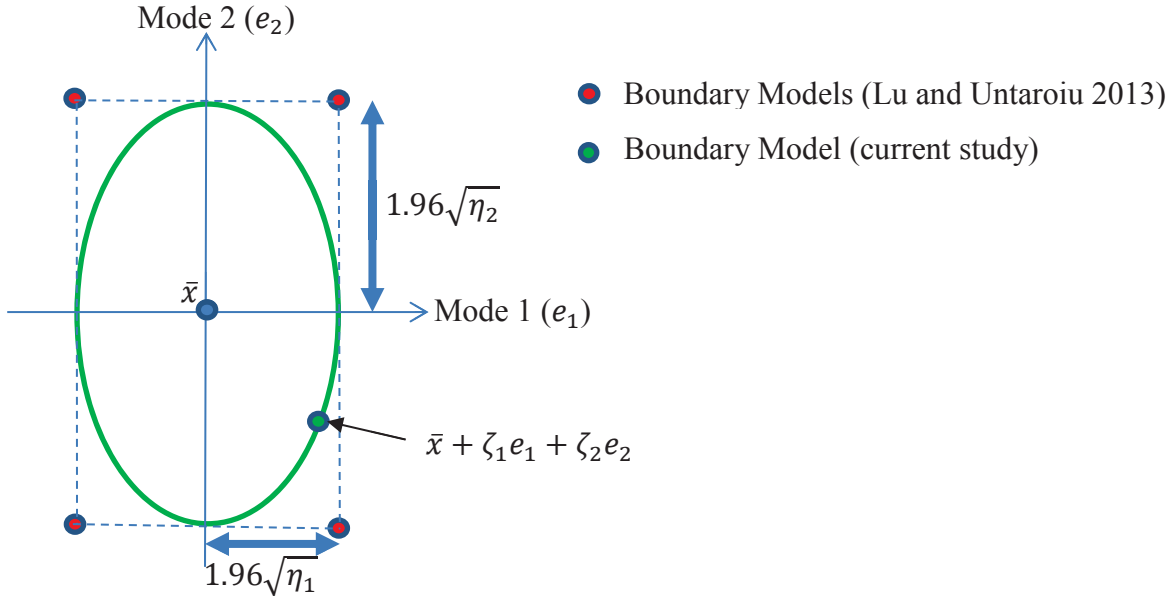
Figure 1. An illustration of the set of 95% statistical boundary models developed using two pre-selected modes ($q=2$).

Note: Each eigenvector e_i (dimension: $3P \times 1$) is not the same as the basis vector of ordinary 2D Euclidian space (dimension: 2×1).

The set of statistical boundary models could be defined as q-hyper-rectangles (Lu and Untaroiu, 2013b) around the mean model, where q is the number of pre-selected orthogonal modes of variation. However, this approach may over predict the boundaries of $\kappa\%$ boundary models, similar to the rectangle approach used to define the boundaries of test data corridors (Lessley et al., 2004; Untaroiu and Lu, 2013). Therefore, in this study, a q-hyper-ellipsoid approach is used to define the set of boundary models (Fig. 1). In this approach, a statistical boundary model ($\hat{x}$) is a point of the q-hyper-ellipsoid and it is defined as:

$$\hat{x} = \bar{x} + \sum_{i=1}^{q} \zeta_i e_i \qquad (7)$$

where ζ_i are shape parameters with q-dimensional elliptical coordinates.

When $q=2$ (Fig. 1), the 2-hyper-ellipsoids equation for 95% boundary models is

$$\sum_{i=1}^{2} \frac{\zeta_i^2}{(1.96\sqrt{\eta_i})^2} = 1 \qquad (8)$$

Therefore, ζ_i are

$$\zeta_1 = 1.96\sqrt{\eta_1}\cos(\delta)$$
$$\zeta_2 = 1.96\sqrt{\eta_2}\sin(\delta) \qquad (9)$$

where $0 \le \delta < 2\pi$.

Sets of ζ_i would be changed according to different q. For example, when $q=5$, the 5-hyper-ellipsoids equation for 95% boundary models is

$$\sum_{i=1}^{5} \frac{\zeta_i^2}{(1.96\sqrt{\eta_i})^2} = 1 \qquad (10)$$

Therefore, ζ_i are

$$\zeta_1 = 1.96\sqrt{\eta_1}\cos(\delta_1)$$
$$\zeta_2 = 1.96\sqrt{\eta_2}\sin(\delta_1)\cos(\delta_2)$$
$$\zeta_3 = 1.96\sqrt{\eta_3}\sin(\delta_1)\sin(\delta_2)\cos(\delta_3)$$
$$\zeta_4 = 1.96\sqrt{\eta_4}\sin(\delta_1)\sin(\delta_2)\sin(\delta_3)\cos(\delta_4)$$
$$\zeta_5 = 1.96\sqrt{\eta_5}\sin(\delta_1)\sin(\delta_2)\sin(\delta_3)\sin(\delta_4) \quad (11)$$

where $0 \le \delta_i \le \pi$ when $i=1,2,3$, and $0 \le \delta_i < 2\pi$ when $i=4$.

By adjusting the shape space, different $\kappa\%$ boundary models can be obtained. For instance, the shape space [-1.65 SD, 1.65 SD] of each mode could be used to develop the "90% boundary models."

Tensile Testing of Human Liver Parenchyma

Uniaxial tensile tests were performed on the parenchyma of three fresh human livers (Table 2). The tissue slicing and stamping procedures were used to obtain constant thickness "dog-bone" shaped liver parenchyma specimens (Kemper et al., 2010; Kemper et al., 2012) commonly used for uniaxial tensile

testing. Fifty-two coupon "dog-bone shape" specimens were cut using a custom blade assembly with the length, middle width and thickness close to 55.5 mm, 10 mm and 5 mm respectively (Fig. 2). The parenchyma specimens without capsule had their longitudinal axis (loading direction) parallel to the liver surface. To maintain specimen hydration until testing, specimens were immersed in a bath of Dulbecco's Modified Eagle Medium (DMEM).

Table 2. Subject information.

Subject ID	Gender (M/F)	Age (years)	Weight (kg)	Stature (cm)
1	M	79	45.4	162.6
2	M	79	81.6	182.9
3	M	76	83.9	172.7
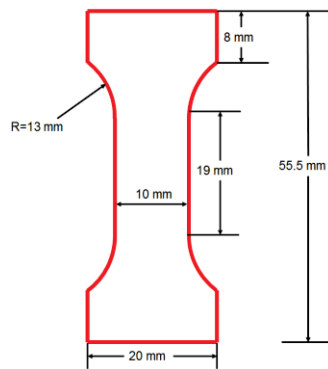
Figure 2. Coupon specimen size.

The tensile testing system consisted of two motor driven linear stages (Parker Daedal MX80S, Irwin, PA) mounted to a vertically oriented aluminum plate (Fig. 3). A uniaxial load cell (Interface, WMC Miniature-22.24N, Scottsdale, AZ) and an accelerometer (Endevco 7264B, 2000 G, San Juan Capistrano, CA) were mounted between the linear actuator and the clamp. The system was operated with a multi-axis controller (Parker ACR9000, Irwin, PA), which provided synchronized motion of both linear stages, and a motor driver (Parker ViX, Irwin, PA). The specimen mounting procedure described previously (Kemper et al., 2010; Kemper et al., 2012) was used to ensure that all specimens had a minimal but consistent preload (i.e. 1 g of tension due to the gravitation). The testing system loaded the specimen by simultaneously moving the top and bottom grips away from one another at a constant velocity. Specimens were divided into four sets, which were tested until failure at the following strain rates: 0.01 s^{-1}, 0.1 s^{-1}, 1.0 s^{-1}, and 10 s^{-1}. A high speed video camera (Phantom V4, Vision Research, Wayne, NJ) with a resolution of 7.7 pixels/mm recorded the

specimen during testing. The data acquisition and video sampling rates for each loading rate are listed in Table 3. The force and displacement time histories were recorded during each test, along with high-speed video. In all tests reported in this study, the failure location was in the gage region of the specimen.

Prior to each test, the 3D geometry of each specimen mounted between clamps was obtained using a FARO Laser ScanArm (Laser Line Probe V3, FARO Technologies, Inc., Lake Mary, Florida) with an accuracy of ±35 µm. The specimens were scanned from different angles in order to acquire a cloud of points, which can approximate reasonably the coupon surface. A poly-surface was obtained from the point cloud of each specimen using Geomagic Studio 11 (Geomagic, Inc, Morrisville, NC) which then was transformed to a Non-Uniform Rational B-Spline (NURBS) surface using Rhino v. 5.0 (Robert McNeel & Associates, Seattle, WA).
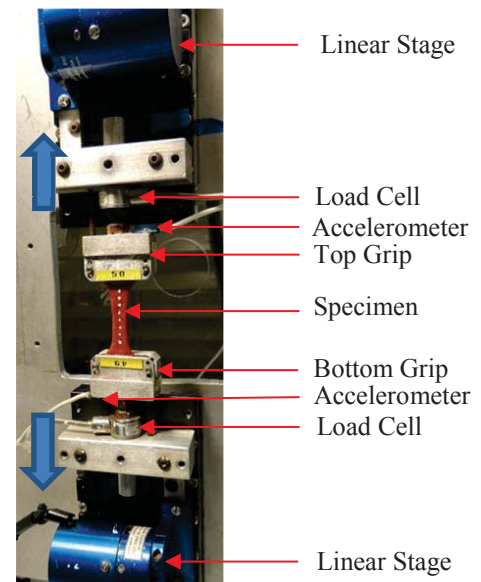

Figure 3. Experimental setup.

Table 3. Data acquisition and video sampling rates by loading rate.

Rate	Desired Strain Rate (s^{-1})	Data Acquisition (kHz)	Video (Hz)
Rate 1	0.01	0.2	20
Rate 2	0.1	2.0	70
Rate 3	1.0	20.0	500
Rate 4	10.0	40.0	1000

The inertia compensated force (F_{IC}) was calculated based on the measured time histories of force (F), grip acceleration (a), and effective mass (m_{eff}) (Eq. 12). The effective mass was defined as half of the load cell mass plus the grip mass between the load cell and specimen. F_{IC} was then fitted by a 5th degree polynomial curve up to the time of failure.

$$F_{IC} = F - a * m_{eff} \qquad (12)$$

The time of tissue failure was defined as the point of the force-time curve where the force reached a maximum and then decreased more than 3% of its peak value.

Identification of Material Properties: Video Data Analysis

A collinear and equidistant pattern of paint (optical) markers was applied to each specimen (Fig. 3) prior to testing with 4 mm between every two markers. Motion analysis software (TEMA Version 2.6, Linkoping, Sweden) was used to track the displacement of these optical markers from recorded videos. The video data displacement was calculated based on the two closest optical markers spanning the location of the tear site. The displacement between these markers was curve fitted with a 5th degree polynomial up to the time of failure. This methodology is consistent with that used by previous studies (Kemper et al., 2010; Kemper et al., 2012).

The stretch ratio (λ) and Green-Lagrangian (GL) strain (ε) were then calculated from the curve fit displacement data as follows:

$$\lambda = \frac{L_n}{L_0} \qquad (13)$$

$$\varepsilon = \frac{1}{2}(\lambda^2 - 1) \qquad (14)$$

where L_0 is the initial distance between the optical markers and L_n is the instantaneous distance between the optical markers. The strain rates were calculated as the slope of the time histories of the strain, correspondingly from 25% to 75% of the peak strain, which is corresponds to the time of failure (Kemper et al., 2010; Kemper et al., 2012).

The 2nd Piola-Kirchhoff (PK) Stress (S) was calculated based on the curve fit inertia compensated force data, the stretch ratio (λ), and initial cross-sectional area (A_0) (Eq. 15). The initial cross-sectional area at the region of the tear was quantified from pre-test pictures.

$$S = \frac{F_{IC}}{\lambda * A_0} \qquad (15)$$

The stress-strain curves were then calculated for each test. The failure stress and failure strain were defined as the stress and strain at the time of failure. Two-way analysis of variance (ANOVA) for testing the effects of strain rates and donors (Table 2) on the mean of the failure stress and failure strain was conducted (α=0.05). Tukey-Kramer multiple comparison tests (α=0.05) were then performed to identify significant differences between strain rates and between donors (α=0.05). In addition, a series of two-sample Mann–Whitney tests (Tallarida and Murray, 1986) for the difference in median were performed to evaluate statistical significance (α=0.05) in failure stress and failure strain between the data in the current study and previously published data (Kemper et al., 2010).

It should be mentioned that through the video analysis the material properties close to the tear site are determined. Our previous study (Untaroiu and Lu, 2013) showed that these regional properties incorporated in specimen-specific FE models do not always predict reasonable the stiffness behavior of tissue during tensile tests. Therefore, an identification of whole specimen material properties was performed, as it is explained in the following section.

Identification of Material Properties: FE-Based Optimization Analysis

Many studies showed that the abdominal solid organ tissues, such as liver, could be reasonably considered as isotropic and incompressible materials (Holzapfel, 2000). The hyperelastic formulation showed to be a good phenomenological constitutive approach within the nonlinear regime of biological tissues (Holzapfel, 2000). The Ogden material model best matched the test data among various hyperelastic models implemented in LS-Dyna v. 6.0 (LSTC, Livermore, CA) (Untaroiu and Lu, 2013) and therefore it was chosen for parameter identification of all specimens in this study. The strain energy function of the Ogden material model (Ogden, 1997) can be expressed as:

$$W(\lambda_1, \lambda_2, \lambda_3) = \sum_{i=1}^{N_d} \frac{\mu_i}{\alpha_i}\left(\lambda_1^{\alpha_i} + \lambda_2^{\alpha_i} + \lambda_3^{\alpha_i} - 3\right) \quad (16)$$

where $\lambda_1, \lambda_2, \lambda_3$ are the principal stretches, N_d is the order of the Ogden material model, μ_i and α_i are ith shear modulus and exponent, respectively. The displacement between the grips was measured during tests using potentiometers attached to the linear stages and then fitted with a 1st degree polynomial to reduce the measurement noise. Two steps were

attempted in this study to identify the parameters (μ_i and α_i) of the Ogden material model (Untaroiu and Lu, 2013) for each strain-rate: 1) analytical-based optimization approach and 2) FE-based optimization approach.

The analytical-based approach was implemented to obtain the initial guess of Ogden material model parameters for the FE-based optimization approach. In this approach, the specimen is approximated as a beam with an average cross-sectional area and the length as the pre-test distance measured between clamps. Therefore, the strain is constant along the specimen based on the isotropy and homogenous assumptions. For an isotropic incompressible material with an applied stretch λ_1 along the loading direction, the stretches along the other directions are

$$\lambda_2 = \lambda_3 = \lambda_1^{-1/2} \qquad (17)$$

The stretch λ_1 can be determined from the displacement data as follows:

$$\lambda_1(t) = \frac{\widetilde{L_n}}{\widetilde{L_0}} \qquad (18)$$

where $\widetilde{L_0}$ is the initial length of specimen, and $\widetilde{L_n}$ is the instantaneous distance between the clamps.

The strain energy function of a first-order Ogden model ($N_d = 1$), as used in the current study, is:

$$W(\lambda_1) = \frac{\mu_1}{\alpha_1}\left(\lambda_1^{\alpha_1} + 2\lambda_1^{-\alpha_1/2} - 3\right) \qquad (19)$$

The nominal (first PK) stress P_1 and the second PK stress S_1 are given by:

$$P_1 = \frac{\partial W}{\partial \lambda_1} = \mu_1\left(\lambda_1^{\alpha_1-1} - \lambda_1^{-\alpha_1/2-1}\right) \qquad (20)$$

$$S_1 = \frac{P_1}{\lambda_1} \qquad (21)$$

Therefore, the time history of the force predicted by the model is:

$$F_m(t) = P_1(\mu_1, \alpha_1, t)\widetilde{A_0} \qquad (22)$$

To be consistent, the cross-sectional area ($\widetilde{A_0}$) was calculated as the average of cross-sectional areas at three locations: the middle location and other 2 locations about 3 mm up and down from the middle location, from pre-test pictures.

The values of the material model parameters (α_1 and μ_1) were optimized using the active-set algorithm in MATLAB v. R2012b (The MathWorks, Inc., Natick,

MA), which tried to minimize the root mean square (RMS) of the differences between the model force to the corresponding test data (Eq. 23).

$$F_{error} = \sqrt{\sum_{i=1}^{n_t}[F_m(t_i) - F_{IC}(t_i)]^2} \qquad (23)$$

where t_i is a series of n_t-time sequences equally distributed from the time when the specimen started to be loaded (time 0) up to the time of failure. The active-set algorithm utilizes a sequential quadratic programming method typically used to solve medium scale optimization problems (problems with reduced number of variables) (Coleman, 2011). The initial values of α_1 and μ_1 were chosen as 10 and 5 kPa.

The FE-based approach employs specimen-specific FE simulations to determine the material model parameters using the displacement data measured at grip locations as the input. The implementation of the strain energy function for the Ogden material model in the FE software, LS-Dyna v. 6.0, has an unconstrained form by adding a hydrostatic work term to the strain energy functional (MAT_77_O, LS-Dyna Manual (Hallquist, 2007)):

$$W(\lambda_1, \lambda_2, \lambda_3) = \sum_{i=1}^{N_d} \frac{\mu_i}{\alpha_i}\left(\lambda_1^{\alpha_i} + \lambda_2^{\alpha_i} + \lambda_3^{\alpha_i} - 3\right) + K(J - 1 - lnJ) \qquad (24)$$

where K is the bulk modulus and J is the volume ratio. The liver parenchyma was assumed as a nearly incompressible material, with a Poisson's ratio of 0.4996 in all models. A tension test was simulated by prescribing the displacement-time histories recorded in testing to the specimen ends. For the tests performed at 0.01 s^{-1} and 0.1 s^{-1} loading rate, implicit FE simulations with a fully integrated element integration scheme were employed. A constant stress element formulation with a viscosity-based hourglass control ($Q_m = 0.02$) was used in all explicit FE simulations (1 s^{-1} and 10 s^{-1} loading rates). A simulation was considered successful if the peak hourglass energy was under 3% of the peak internal energy.

The material parameters (μ_1, α_1) calculated from the analytical-based approach were considered as input variables, and the RMS of forces between the test data and corresponding model data was defined as the objective function to be minimized (Eq. 23). The successive response-surface methodology (SRSM), an iterative statistical optimization method implemented in LS-Opt v. 4.2 (LSTC, Livermore, CA), was used to find a set of parameters which minimized the objective function. A D-optimal design was used to search the test points around the

optimum point determined after each iteration and a quadratic response surface was fit through the values of objective function calculated from FE simulation (Untaroiu, 2010). The optimum point obtained using the analytical model was considered as the initial point, and the optimization process was stopped after 6 iterations. The ground-state shear modulus μ is then be determined by (Hu et al., 2011):

$$\mu = \frac{\mu_1 \alpha_1}{2} \qquad (25)$$

Characteristic Average and Variation Corridor

The 2nd PK stresss-GL strain curves were calculated using Eq. 20 and 21, based on the Ogden material parameters, μ_1 and α_1, obtained from the FE-based approach. For each specimen, the end (failure) point of the stress-strain curve was determined based on the maximum GL strain extracted from the FE simulation of specific-specimen model with optimized Ogden parameter at the time of failure. Then, the average curves and their corresponding variation corridors were calculated for each strain rate using a normalization technique (Lessley et al., 2004). This technique begins with a method for averaging specimen stress-strain responses in which curve shape characteristics are maintained and discontinuities are avoided. Individual responses sharing a common characteristic shape are averaged based upon normalized strain values. The normalized average response is then scaled to represent the given data set using the mean peak strain value associated with the set of experimental data. Some applications and justification of this technique were previously published (Lessley et al., 2004; Untaroiu and Lu, 2013). The Ogden model parameters of the average curve, denoted as (μ_1^*, α_1^*), were then identified using the same methodology employed for material identification of each specimen by analytical-based approach. An elliptical corridor approach was used to account for variability in both stress and strain coordinates along the average curves (Untaroiu and Lu, 2013). The boundaries of the elliptical corridor were obtained as an envelope of the ellipsoids defined along the average curves using 1 standard deviation (± 1 SD) as ellipsoid axes (Untaroiu and Lu, 2013).

Stochastic Optimization

After stress-strain corridors ("test" corridors) were determined for each loading rate, a stochastic

optimization was performed to calculate the SD of the model parameters (μ_{1SD}, α_{1SD}). Since reduced number of stress-strain curves may influence their statistical values, an iterative adjustment process of their values was performed. In this process, three parameters, μ_{1SD}, α_{1SD}, and ε_{fSD} (the SD of the failure GL strain), were assumed mutually independent and their values were identified by optimization. First, a set of parameters, (μ_1^S, α_1^S) where $S=1,...,N_{opt}$ (N_{opt} was chosen as 1000 in this study), was generated using (μ_1^*, α_1^*) and their assumed SD (μ_{1SD}, α_{1SD}). A Latin Hypercube Sampling (LHS) approach was employed with the initial values of α_{1SD} and μ_{1SD} chosen as 0.1 and 1 kPa, respectively. Then, a set of failure GL strain values (ε_f^S), coupled with each S in the set (μ_1^S, α_1^S), was determined from a normal distribution with the mean failure GL strain (ε_f^*) calculated from the FE-based approach by rates and their assumed SD (ε_{fSD}). The initial SD of the failure GL strain was calculated based on the failure GL strains of specimens extracted from FE optimized simulations. The stress-strain curves corresponding to this set $(\mu_1^S, \alpha_1^S, \varepsilon_f^S)$ were generated using Eq. 20 and 21, and then the elliptical corridor of the new stress-strain curves, which is called "simulation corridor", was calculated. Finally, the "simulation corridor" was compared to the "test corridor", and the active-set optimization algorithm in MATLAB v. R2012b (The MathWorks, Inc., Natick, MA) was used to minimize the RSM between the curves of "simulation" and "test" corridors. Thus, the optimized SD values of the Ogden model parameters (μ_{1SD}, α_{1SD}) and the failure GL strain value (ε_{fSD}) were reported as statistical parameters of the material model of human liver parenchyma.

RESULTS

Statistical Shape Analysis

The statistical size and shape models of human liver were constructed using PCA. Overall, the first five modes accounted for 67.27% of the global variation (Fig. 4), so only these modes were chosen to graphically represent the overall geometric variability of human liver. The LM-ICP registration method used to align all 15 livers requires CPU time of about 10 minutes on Microsoft Windows workstations equipped with Intel Pentium Dual 3.10GHz processors.

The liver size and shape models were plotted for -3SD, mean, and +3SD for the first five modes, which contributed more than 60% of the overall variation (Fig. 5). The height of the right lobe was found to exhibit the most significant variation (24.9%) (Fig. 5, Mode 1). Changes of the thickness of the right lobe were found in the second mode (Fig. 5, Mode 2), which represented 14.2% of the global variance. The third mode of variation represented 11.1% of the global variability and corresponded to the variation of the thickness of left lobe (Fig. 5, Mode 3). The fourth mode of variation represented 9.8% of the entire variance, and the curvature of liver was found to be the main difference between the shape models in this mode (Fig. 5, Mode 4). Finally, the angle of right and left lobes from the medial view and the height of left lobe were found to be the variations on the fifth principal component mode, accounting for 7.2% of the overall variation (Fig. 5, Mode 5).
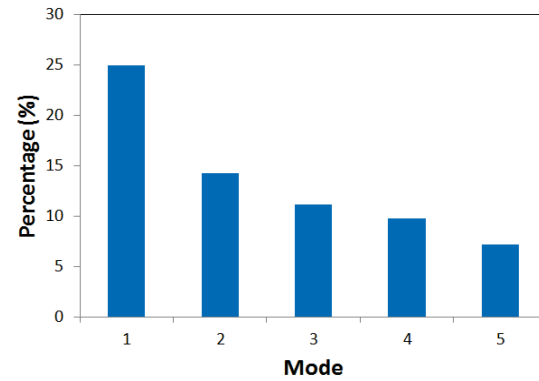
Figure 4. Percentage of variation contributed by each mode for the human liver statistical size and shape model.
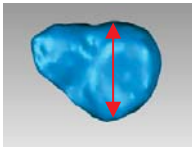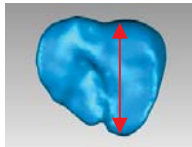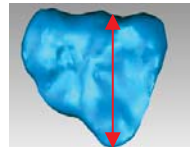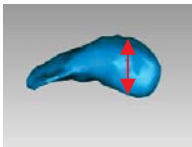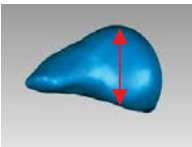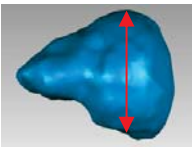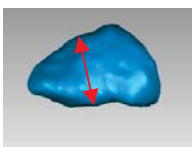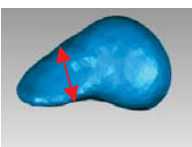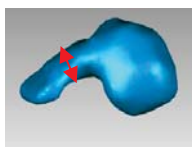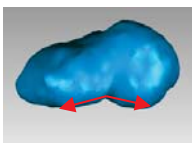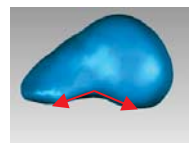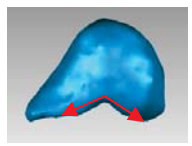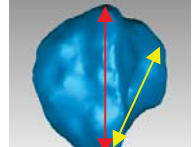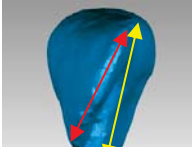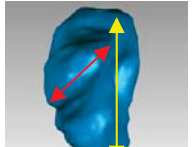
Mode	-3 SD	Mean Shape	+3 SD	Variation	Description
1				24.9%	Height of right lobe
2				14.2%	Thickness of right lobe
3				11.1%	Thickness of left lobe
4				9.8 %	Curvature of liver
5				7.2 %	Angle of right and left lobes and height of left lobe

Figure 5. The first five modes of variation of human livers.

The modes used for the construction of the statistical boundary models were described by a set of principal component score distributions. These score distributions, corresponding to the first five modes of human liver, were standardized by their means and SD (Fig. 6). All p-values from the Kolmogorov–Smirnoff test on the similarity between the standardized principal component scores and a standard normal distribution were greater than 0.05 (Fig. 6). This indicates that the distributions of the principal component scores were not significantly different from a normal distribution for all five modes in human livers.

The surfaces of the mean and other two 95% boundary models of the human liver were constructed (Fig. 7). These boundary models correspond to 1) $\delta_1 = \delta_2 = \delta_3 = \delta_4 = \pi/4$, and 2) $\delta_1 = \pi$, $\delta_2 = \delta_3 = \delta_4 = 0$ (Eq. 11). No linear correlations were observed between the variations of the boundary models, as is assumed by traditional scaling methods used frequently to develop percentile models.
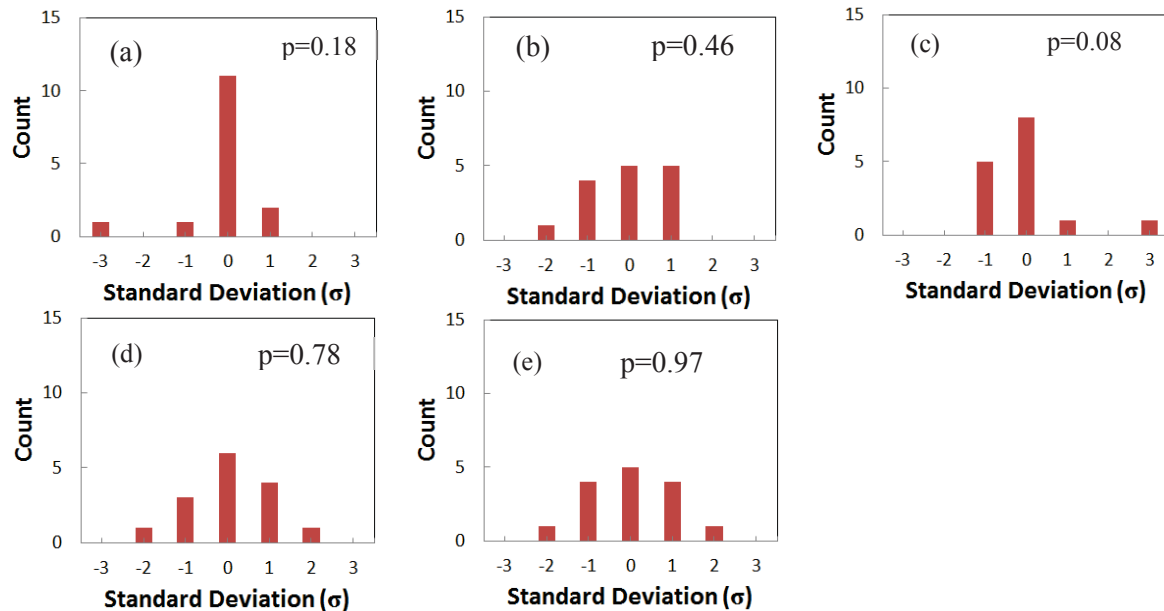
Figure 6. Distribution of shape parameters of the first five modes of human liver (a) Mode 1; (b) Mode 2; (c) Mode 3; (d) Mode 4; (e) Mode 5. p represents p-value resulting from a Kolmogorov–Smirnoff test on the similarity between standardized principal component scores and a standard normal distribution. p-values>0.05 represent normally distributed shape parameters.

Figure 7. Mean and two selected boundary models of human liver, developed using the first five principal component modes (a) Mean shape; (b) Statistical boundary model #1; (c) Statistical boundary model #2.

Figure 8. High-speed video stills of a typical uniaxial tensile test (Rate 2: 0.1 s^{-1}).
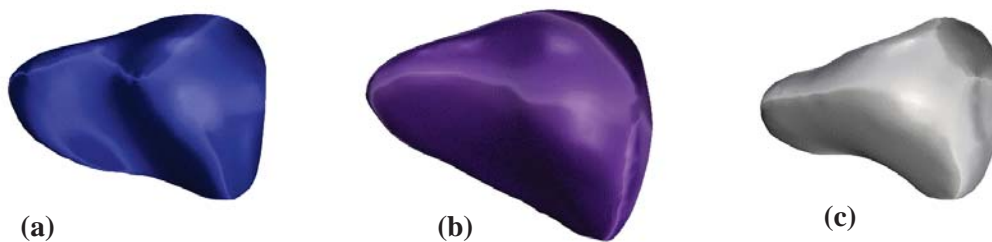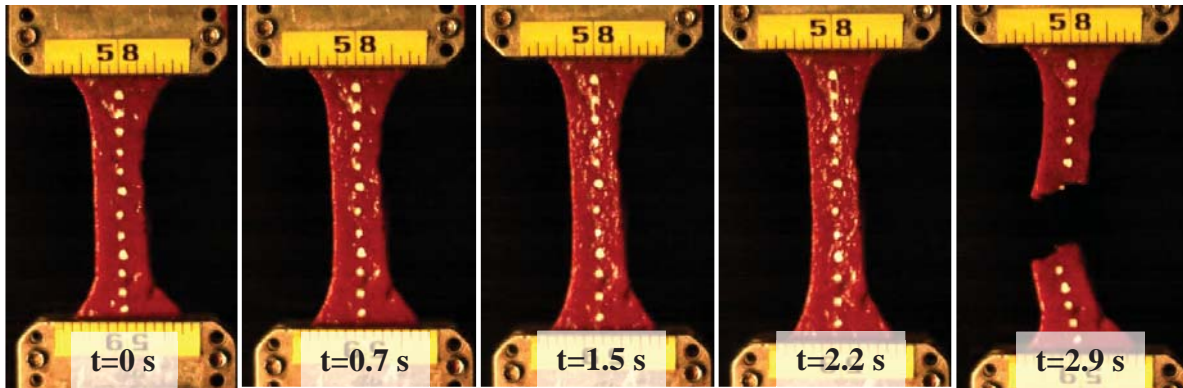
Identification of Material Properties: Video Data Analysis

A typical uniaxial test until failure is shown in Fig. 8. The stress-strain curves by loading rate obtained from 52 tensile testing specimens are shown in Fig. 9. The calculated average strain rates were 0.008 s^{-1}, 0.076 s^{-1}, 0.747 s^{-1}, and 9.682 s^{-1} for specimens tested at 0.01 s^{-1}, 0.1 s^{-1}, 1.0 s^{-1}, and 10.0 s^{-1}, correspondingly. The data show that when the loading rate increased, the failure stress increased and the failure strain decreased. The number of samples in each group is shown in Table 4.

The two-way ANOVA for testing the effects of strain rates and donors showed that the means of failure strain and failure stress were significantly different between strain rates (p=0.034 and p=0.026,

correspondingly), and the means of failure strain were significantly different between donors (p=0.006) (Tale 5). No significant interaction effects were found between strain rates and donors (p=0.282 and p=0.988 for failure strain and failure stress, correspondingly). Multiple comparison tests showed significant differences (p<0.05) in the means of failure strain and failure stress only between Rate 1 and Rate 4 specimens. In addition, the mean failure strain of Subject #1 specimens was significantly lower than those from the other two donors (p<0.05). Furthermore, two-sample Mann–Whitney tests showed that no significant differences were found in terms of failure properties between data in the current study and the data reported previously (Kemper et al., 2010) for corresponding rate and stress/strain combinations (p>0.05) (Fig. 10).

Table 4. Averages and standard deviations by loading rate.

Rate	# of samples	Desired Strain Rate (s^{-1})	Average Strain Rate (s^{-1})	Average Failure Stress (kPa)	Average Failure Strain (strain)
Rate 1	14	0.01	0.008 (±0.001)	41.32 (±13.87)	0.305 (±0.088)
Rate 2	13	0.1	0.076 (±0.012)	44.72 (±7.08)	0.275 (±0.064)
Rate 3	12	1.0	0.747 (±0.129)	46.25 (±11.49)	0.264 (±0.055)
Rate 4	13	10.0	9.682 (±2.487)	56.89 (±15.48)	0.245 (±0.037)

Table 5. Two-way ANOVA for testing the effects of strain rates and donors on the mean of the failure strain and failure stress. Bold: p-value<0.05.

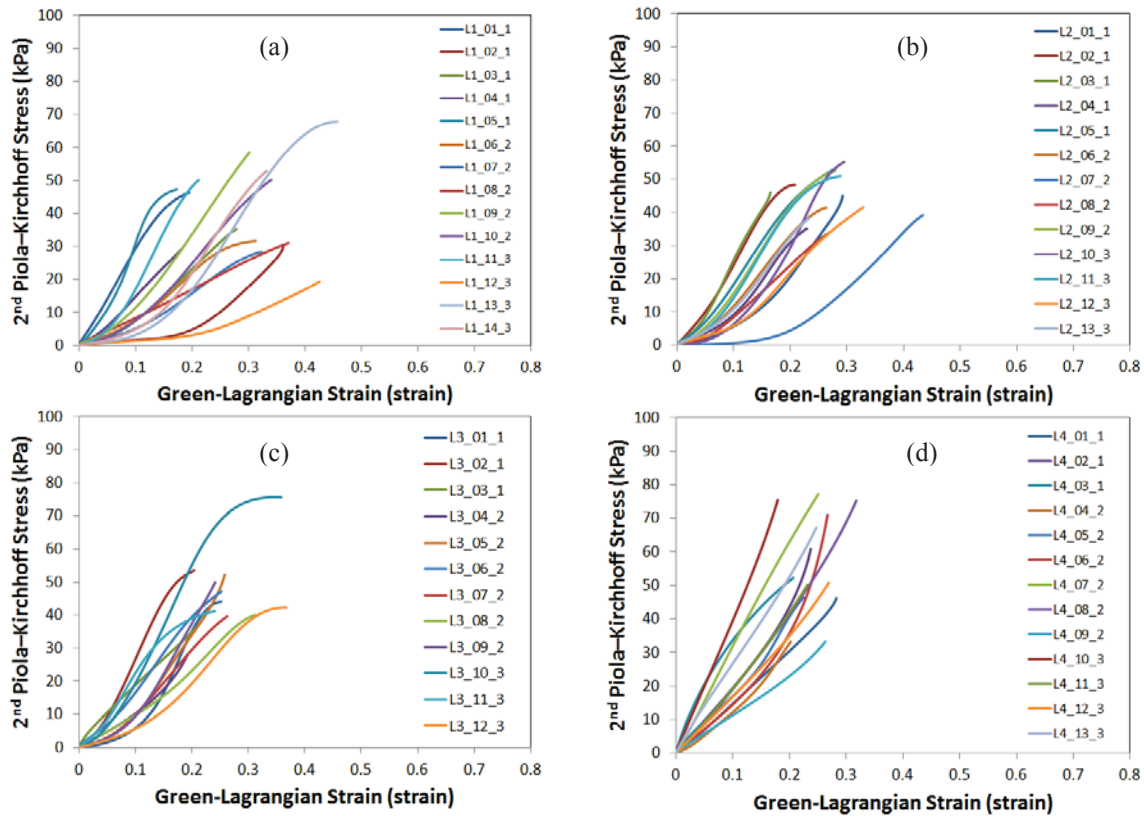| Failure Strain	F-value	p-value
Strain Rate	3.18	**0.034**
Donor	5.89	**0.006**
Rate and Donor Interaction	1.29	0.282
Failure Stress	**F-value**	**p-value**
Strain Rate	3.43	**0.026**
Donor	1.32	0.280
Rate and Donor Interaction	0.15	0.988

Figure 9. Stress vs. strain curves (a) Rate 1: 0.01 s^{-1}; (b) Rate 2: 0.1 s^{-1}; (c) Rate 3: 1 s^{-1}; (d) Rate 4: 10 s^{-1}. The last digit of each specimen ID is the donor subject ID.
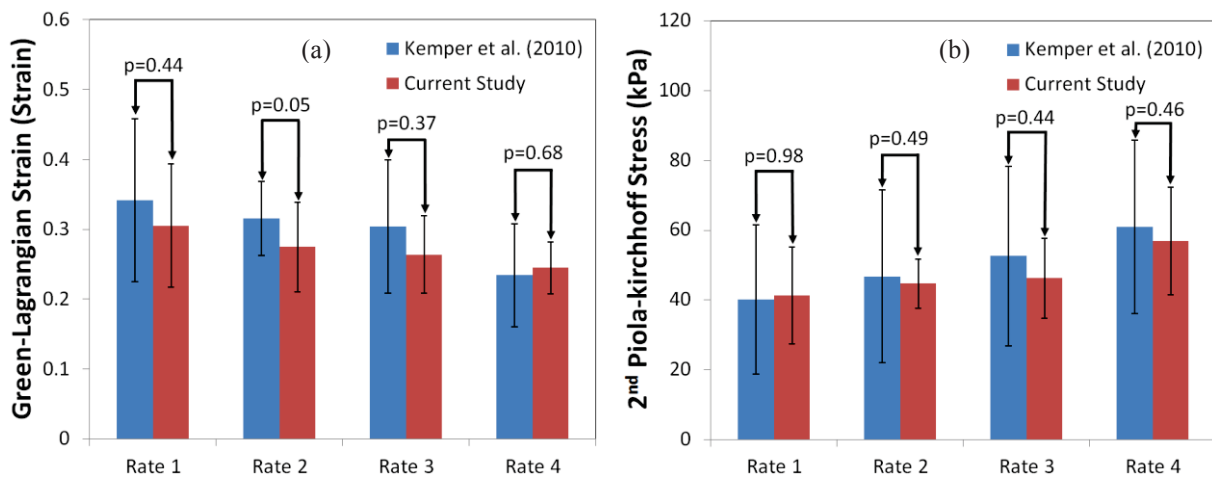

Figure 10. Comparisons of failure properties between current study and Kemper's study (Kemper et al., 2010) (a) Green-Lagrangian strain; (b) 2nd Piola-Kirchhoff stress.

Identification of Material Properties: FE-Based Optimization Analysis

The average ground-state shear modulus μ increased from 27.05 to 36.27 when the strain rate increased from 0.01 s^{-1} to 10.0 s^{-1}. The optimal material model parameter α_1 ranged from 0.88 to 26.32, and μ_1 ranged from 6.72 to 16.47 kPa (Table 6). Good correlations (R^2>0.99) were observed between the force time histories of the specimen-specific models with the material parameters obtained by FE-based approach and corresponding test data, indicating the good model fittings of the Ogden material model.

All specimens failed completely in the gauge length of the coupons. A failure criterion was not defined in the subject-specific FE model, but the highest values of GL strain (along the loading direction) were always observed in the gauge length (Fig. 11).

The characteristic averages and the variation corridors of the stress-strain curves calculated for each loading rate are shown in Fig. 12. The slopes of the average curves became larger when increasing the strain rates, indicating the stiffer responses at higher strain rates.

Stochastic Optimization

The SD of the model parameters $(\mu_{1SD}, \alpha_{1SD})$ obtained by the stochastic optimization process are presented together with the parameters of average curves (μ_1^*, α_1^*) in Table 7. α_1^* ranged from 9.123 to 10.133, and μ_1^* ranged from 5.686 to 6.823 kPa. The mean failure GL strain (ε_f^*) obtained by the FE-based approach decreases from 0.431 to 0.370 as loading rate increases. The standard deviation of the failure GL strain (ε_{fSD}) ranged from 0.055 to 0.071. The "test" and optimized "simulation" corridors, along with their characteristic averages, based on 1000 LHS samples, are plotted in Fig. 13.
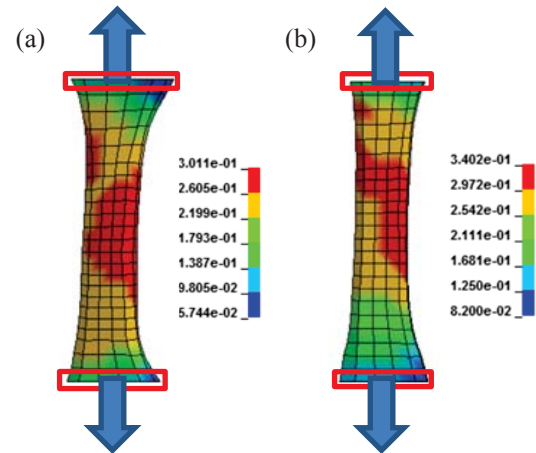
Figure 11. The distribution of Green-Lagrangian strain before failure for typical samples at high rate tensile tests. FE model with specimen-specific FE-based material parameters (a) Rate 4 (specimen L4_02_1); (b) Rate 3 (specimen L3_03_1). Red boxes represent the locations of boundary conditions.
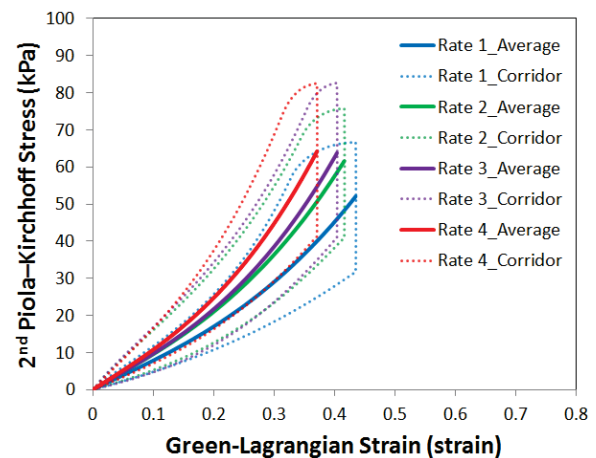

Figure 12. Characteristic averages and variation corridors by rates based on the Ogden material models from specimen-specific FE simulations.

Table 6. Ogden material parameters.

Rate 1	α_1	μ_1	μ	Rate 2	α_1	μ_1	μ	Rate 3	α_1	μ_1	μ	Rate 4	α_1	μ_1	μ
L1-01_1	9.55	8.86	42.31	L2-01_1	7.90	9.73	38.43	L3-01_1	7.52	10.56	39.67	L4-01_1	10.49	8.12	42.57
L1-02_1	3.27	10.95	17.91	L2-02_1	22.73	6.79	77.15	L3-02_1	26.32	7.06	92.85	L4-02_1	12.71	10.12	64.33
L1-03_1	7.77	6.72	26.12	L2-03_1	12.35	8.24	50.89	L3-03_1	14.39	7.15	51.47	L4-03_1	16.64	7.44	61.95
L1-04_1	3.75	14.62	27.39	L2-04_1	6.97	10.86	37.87	L3-04_2	2.29	11.99	13.74	L4-04_2	5.02	10.82	27.15
L1-05_1	5.21	13.25	34.54	L2-05_1	9.74	9.90	48.19	L3-05_2	3.64	9.80	17.84	L4-05_2	6.44	11.40	36.71
L1-06_2	6.91	7.70	26.61	L2-06_2	6.68	7.56	25.25	L3-06_2	5.81	8.86	25.75	L4-06_2	4.79	10.19	24.41
L1-07_2	5.25	7.26	19.06	L2-07_2	5.06	9.82	24.86	L3-07_2	5.08	9.24	23.45	L4-07_2	5.77	11.53	33.26
L1-08_2	3.91	7.70	15.04	L2-08_2	3.71	9.54	17.69	L3-08_2	9.55	7.98	38.09	L4-08_2	7.56	9.95	37.62
L1-09_2	9.44	8.02	37.82	L2-09_2	7.44	8.33	30.98	L3-09_2	2.91	14.14	20.61	L4-09_2	4.66	8.83	20.57
L1-10_2	6.86	8.55	29.32	L2-10_3	4.77	9.96	23.75	L3-10_3	5.28	11.19	29.57	L4-10_3	6.87	9.38	32.24
L1-11_3	6.57	10.07	33.06	L2-11_3	4.63	9.83	22.75	L3-11_3	3.11	12.01	18.66	L4-11_3	4.50	11.29	25.39
L1-12_3	0.88	16.47	7.21	L2-12_3	4.44	9.75	21.68	L3-12_3	5.90	10.25	30.23	L4-12_3	4.41	10.41	22.97
L1-13_3	6.63	9.14	30.27	L2-13_3	2.21	13.90	15.38					L4-13_3	7.83	10.82	42.37
L1-14_3	8.28	7.74	32.03												
Mean	**6.02**	**9.79**	**27.05**	**Mean**	**7.59**	**9.56**	**33.45**	**Mean**	**7.65**	**10.02**	**33.49**	**Mean**	**7.52**	**10.02**	**36.27**
SD	**2.47**	**2.99**	**9.48**	**SD**	**5.28**	**1.73**	**17.19**	**SD**	**6.77**	**2.13**	**21.56**	**SD**	**3.70**	**1.27**	**13.89**

Note: Units: μ_1 (kPa) and μ (kPa).

Table 7. Stochastic optimization of Ogden material parameters and failure strain by loading rate.

Rate	Average			Standard Deviation		
	α_1^*	μ_1^* (kPa)	ε_f^*	α_{1SD}	μ_{1SD} (kPa)	ε_{fSD}
Rate 1	9.123	5.686	0.431	0.502	1.018	0.071
Rate 2	9.393	6.665	0.414	0.272	1.342	0.063
Rate 3	9.871	6.282	0.403	0.317	0.975	0.061
Rate 4	10.133	6.823	0.370	0.324	0.946	0.055
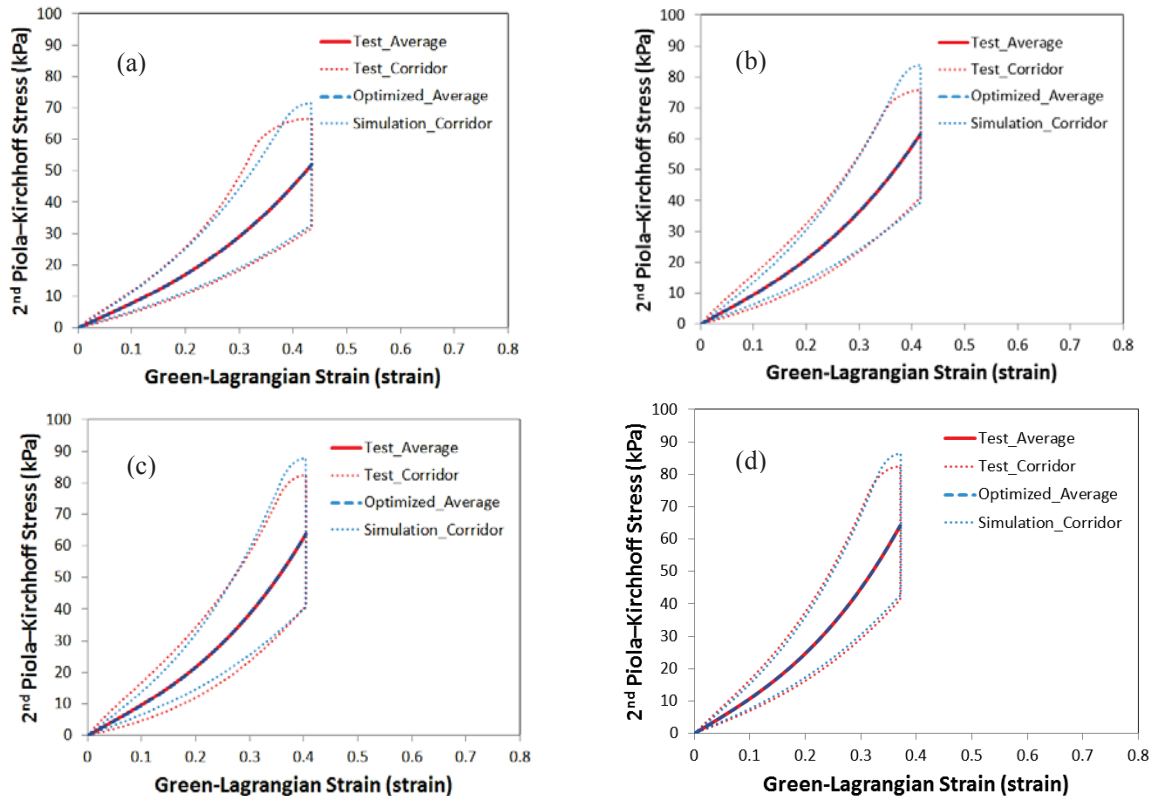
Figure 13. Stochastic optimization: comparisons between test and simulation corridors (a) Rate 1; (b) Rate 2; (c) Rate 3; (d) Rate 4.

DISCUSSION

Although the variations of human liver geometry have been investigated in a few previous studies, the subjects' liver scans in these studies were obtained at supine position or the scanning postures were not specified. The first three variation modes of liver shape presented in this study are different from the corresponding modes reconstructed from subjects in supine postures (Lamecker et al., 2002). These differences could be explained by the shape changes of the abdominal organs between supine and seated postures reported previously (Beillas et al., 2009; Hayes et al., 2013a) or by a different population.

Other previous studies on liver shape models focused on the development of new correspondence methodologies (Chen and Shapiro, 2009) or multi-level statistical shape analysis (Okada et al., 2007; Reyes et al., 2010). Therefore, the liver scans utilized to construct shape models were from patients at supine postures, and the modes of variation were not clearly defined. The current study fully investigates for the first time the liver shape variations based on seated posture models. The proposed approaches, and the strategies could be also applied to other abdominal solid organs such as kidney and spleen.

In this study, the normalization of the training shapes was not considered. Two main reasons for the normalization (Azouz et al., 2006) are: (1) Normalization isolates the shape variation from the height variation; (2) Normalization improves the correspondences between the models because if the models are at the same height, their anatomical components tend to align better with each other. Several studies have normalized the training shapes of their models such as hippocampus (Dalal et al., 2007), patella bone (Fripp et al., 2005), and pancreas (Reyes et al., 2010), while other studies did not consider the normalization scaling on their shape model applications such as tibia (Bredbenner et al., 2010), spine (Lorenz and Krahnstover, 1999), and liver (Lamecker et al., 2002). The current study did not incorporate the normalization of the training shapes because the size variation of the liver models should be considered for constructing the crash test FE abdominal models.

An optimization technique for improving the correspondence, called "iterative landmark sliding" (SLIDE), had been proposed recently (Dalal et al., 2007). The approach has shown to be better than MDL and spherical harmonics (SPHARM), in terms of three shape model evaluation measures (compactness, generalization, and specificity). While the SLIDE optimization was not considered in the current study, it has been shown that the correspondence map established using coordinates and surface normals along with iterative TPS to refine landmarks is sufficient to obtain similar results of refined landmarks (He et al., 2010). In addition, it was also shown that the iterative TPS approach requires less computational time, and all the corresponding landmarks are on the original surface without sliding away(He et al., 2009; He et al., 2010). Moreover, the CPU time for the registration and correspondence process with SLIDE optimization was considerably high (4.6 hours on Microsoft Windows workstations equipped with Intel Pentium Dual 2.16GHz processors) for their hippocampus models, whose geometry were simpler than the liver models(Dalal et al., 2007). The LM-ICP registration and correspondence process in our 15 liver models without the SLIDE optimization required less than 30 minutes. Therefore, considering efficiency and accuracy, the SLIDE optimization may not be required, but the comparison of correspondence maps with SLIDE and without SLIDE is suggested to be investigated in future studies.

The non-linear shape variations between 5%, 50% and 95% liver models (Fig. 7) indicate that the traditional scaling technique based on geometry parameters such as height and width may not be suitable for constructing percentile anthropometric models. This scaling technique has been extensively applied in crash test dummies (Untaroiu et al., 2008; Vezin and Verriest, 2005). The mesh of HUMOS2 model was scaled to any percentile in driving position through only 10 (external) parameters (Vezin and Verriest, 2005). The Polar-II FE model was scaled in vertical direction to match the stature (height) and in the transverse plane to match the total mass between the pedestrian dummy model and subjects, in order to create 5th female, 50th female, and 95th male FE models (Untaroiu et al., 2008). The current study demonstrated that the changes between 5%, 50% and 95% are irregular and non-linear, thus the proposed boundary models provide a better perspective on human variations than the traditional percentile models. While several studies have investigated the shape models of bones (e.g. pelvic bone (Lamecker et al., 2006)) or soft tissues (e.g. brain ventricle (Brett and Taylor, 2000)) represented by each single principle component, the current study is the first study which combines the most significant five shape modes to construct mean and boundary liver models. This technique could be applied to other human tissues and the resulting shape models could be further used to investigate the biomechanical response corridors (Untaroiu et al., 2008).

To investigate the variations of the material properties of liver parenchyma, uniaxial tensile tests were performed *in vitro* at four different loading rates (0.01 s^{-1}, 0.1 s^{-1}, 1 s^{-1} and 10 s^{-1}) on samples extracted from three fresh human livers. A typical non-linear behavior was observed in the structural properties of liver parenchyma with a convex toe region followed by an almost linear region. In addition to these regions, a concave shape close to the pre-failure region was observed especially for low rate tests (0.01 s^{-1}, 0.1 s^{-1}). All these curve features are similar to those tensile tests reported previously for porcine liver (Uehara, 1995), bovine liver (Untaroiu and Lu, 2013), and human liver (Kemper et al., 2010). A phenomenological hyperelastic model (Ogden) with two parameters showed a good overall fit to experimental data. While a better fit could hypothetically be obtained in the future by increasing the complexity of the material model, a complex material model could also increase the number of unknown parameters and consequently the computational effort.

The image-based method (video data analysis), utilized to calculate the material and failure properties, focused on the material responses on the failure (tearing) site of the coupon specimens (Kemper et al., 2010; Untaroiu and Lu, 2013). This method characterizes only the regional properties of the specimens by ignoring the displacement field of all the dots. A digital image correlation (DIC) and dense speckle patterns (Gao and Desai, 2010), could be used to better estimate the strain field in future studies.

One of the main goals of employing the specimen-specific FE approach and obtaining its failure parameters in this study was to obtain the material model parameters, which could be applied to liver parenchyma FE models in common commercial FE software packages such as LS-Dyna. It should be mentioned that previous studies (Ahmed and Beckingham, 2007) showed that material identification using an analytical approach is prone to errors due to the approximation of specimen geometry and differences between the analytical and FE implementation of a certain material model. A nearly incompressible material model of the liver parenchyma could be easily defined using MAT_181 in LS-Dyna v. 6.0, based on the average stress-strain curves reported in this study. This LS-Dyna material model uses a tabulated formulation of hyper-elasticity with rate effects and shows good capability in various numerical validations (Kolling et al., 2007). Compared to the classical hyper-viscoelastic formulations which include viscous terms that require

complex and time consuming parameter identification methods (Ahmed and Beckingham, 2007; Untaroiu, 2005; Untaroiu, 2013), the tabulated stress-strain formulation is undoubtedly more computational efficient (Kolling et al., 2007).

The averages and standard deviations of the Ogden material parameters determined by the stochastic optimization approach (Table 7) were different from those directly calculated from the material parameters of specimens (Table 6). This is because the stochastic optimization approach is used to obtain the averages and standard deviations from the "average stress-strain curves" and "corridors" (Table 7), rather than directly calculating the average and standard deviations of model parameters (Table 6). The averages and standard deviations in Table 6 could be sensitive to outliers, and the standard deviations could be overestimated. Therefore, it is suggested to determine the average curve and corridors first, and then implement the stochastic optimization.

The failure location in testing was generally in the region with high values of stress/strain observed in FE simulations, which may suggest that the stress/strain failure criteria could well predict the occurrence of tears. However, more validations against more complex impact tests, which will ideally include the whole liver, are suggested in the future. A modeling approach for the complex propagation of tears should be also investigated in the future. In addition to the traditional way of modeling failure (i.e. , the element elimination) the application of new modeling approaches such as cohesive zone modeling (Geißler et al., 2010; Gokgol et al., 2012) and the extended FE method (XFEM) (Menk and Bordas, 2010; Pannachet et al., 2009) are recommended to be investigated as well.

In addition to the isotropy and incompressibility assumptions mentioned previously, this study also has several other limitations on the material testing. The Ogden model, as all other hyperelastic models, allows an unrealistic continuous increase of strain energy with the increased strain. While the post-failure behavior was not investigated in this study, combining the continuum damage mechanics (CDM) with the existing hyperelastic models (Volokh, 2010) in the future may help in better prediction of pre- and post-failure behavior of human soft tissues. The test data provided in this study were only obtained from three livers, performing additional tests on specimens obtained from more donors will provide a more accurate material characterization of human liver parenchyma. Furthermore, the Kolmogorov–Smirnoff tests used for the examination of the normality of the

principal component scores may be influenced by the relative small sample size. This is especially true when marginal significance is observed (e.g. p-value=0.08). Therefore, it is suggested in future studies to use larger sample size to construct statistical shape models to avoid the possible bias caused by the size of the samples.

A material model proposed in this study was based on data recorded in tensile tests. However, during crash events, the abdomen may also be subjected combined tension, compression and shear loading due to the contact with the belt system or other vehicle interior parts (e.g. steering wheel for both belted and unbelted occupants). This loading is transferred to the abdominal organs, and may result into complex stress distribution within the liver parenchyma. Therefore, the identification of mechanical and failure properties of liver parenchyma under other loading conditions (e.g. compression and shear) is recommended in future tissue tests. These additional material data could be combined with data presented in the current study to develop deterministic and stochastic material models of parenchyma which may be used in human FE models (Vavalle et al., 2013) to optimize the restraint systems in vehicles (Adam and Untaroiu, 2011; Untaroiu and Adam, 2013).

Under physiological conditions, the liver is perfused with blood, which may add some dilatation that is not present in the un-perfused liver parenchyma specimens. It was also reported that under quasi-static indentation loading, the un-perfused liver is stiffer and more viscous than the liver in vivo (Kerdok et al., 2006). However, no in vivo data exist for dynamic loading conditions especially in failure, so the effects of perfusion on dynamic material properties of liver should be addressed in future studies.

It is well known that the amount of change in the material properties during sample preparation or excision cannot be quantified. Therefore, non-destructive experimental methods (e.g. indentation, aspiration ultrasonic tests) should be performed in the future for better *in-vivo* characterization of liver and comparison with the classical tensile tests.

The hepatic capsule surrounding the liver is a tough fibrous and thin layer enriched with collagen and elastin. To develop a probabilistic FE model of human liver, the thickness and the material model of liver capsule should be also characterized statistically and then assigned to a layer of shell elements surrounding the parenchyma solid elements.

However, the fine layer of the liver capsule may not be easily reconstructed from medical image scans, so new methods should be developed for quantifying the variation in thickness of liver capsule. It is also known that the liver capsule has higher stiffness than liver parenchyma (Hollenstein et al., 2006; Kemper et al., 2010). Therefore, the statistical distributions of the liver capsule properties should be investigated in the future in order to develop probabilistic liver FE models.

The current study presents the first steps in statistical modeling of human organs. The variations of the liver shape and material properties of liver parenchyma presented in this study could be easily implemented in probabilistic FE models of liver which may help to better understand the variations in biomechanical and injury response of liver during impact events (Untaroiu, 2010). In addition, the methodology presented could be applied to other abdominal organs or human regions in the effort to develop a full statistical human model which would provide safety researchers with a powerful tool for better understanding the abdominal injuries (Elhagediab and Rouhana, 1998; Untaroiu et al., 2012) and consequently for designing optimal restraint systems (Adam and Untaroiu, 2011; Untaroiu and Adam, 2013).

CONCLUSION

The first five modes of the liver statistical shape model were presented in this study. The established mean and boundary models could be used in development of future statistical FE models of livers. This study also presents a total of 52 uniaxial tensile tests performed at four different loading rates on fresh specimens of human liver parenchyma. Overall, the failure stress and slopes of the average stress-strain curves increased with increased loading rates, while the failure strain decreased with increased loading rate. A complex stochastic optimization was employed to obtain Ogden material model parameters of liver parenchyma in a statistical formulation. The statistical models in terms of geometry and material properties could be implemented in a future probabilistic model needed to better understand the liver injuries during crashes.

REFERENCES

Adam, T., Untaroiu, C.D., 2011. Identification of occupant posture using a Bayesian classification methodology to reduce the risk of injury in a collision. Transportation Research Part C: Emerging Technologies, 19(6): 1078-1094.

Ahmed, I., Beckingham, I.J., 2007. Liver trauma. Trauma, 9(3): 171-180.

Arajarvi, E., Santavirta, S., Tolonen, J., 1987. Abdominal injuries sustained in severe traffic accidents by seatbelt wearers. J Trauma, 27(4): 393-7.

Azouz, Z.B., Rioux, M., Shu, C., Lepage, R., 2006. Characterizing human shape variation using 3D anthropometric data. Vis. Comput., 22(5): 302-314.

Bah, M.T., Browne, M., 2004. Failure of the cement mantle in hip implants: a probabilistic approach, Transactions of the 50th Annual Meeting of the Orthopaedic Research Society, pp. 1430.

Barratt, D.C. et al., 2008. Instantiation and registration of statistical shape models of the femur and pelvis using 3D ultrasound imaging. Med Image Anal, 12(3): 358-74.

Beillas, P., Lafon, Y., Smith, F.W., 2009. The effects of posture and subject-to-subject variations on the position, shape and volume of abdominal and thoracic organs. Stapp Car Crash J, 53: 127-54.

Belongie, S., Malik, J., Puzicha, J., 2002. Shape matching and object recognition using shape contexts. Pattern Analysis and Machine Intelligence, IEEE Transactions on, 24(4): 509-522.

Besl, P.J., McKay, H.D., 1992. A method for registration of 3-D shapes. Pattern Analysis and Machine Intelligence, IEEE Transactions on, 14(2): 239-256.

Bhatia, K.K., Hajnal, J.V., Puri, B.K., Edwards, A.D., Rueckert, D., 2004. Consistent groupwise non-rigid registration for atlas construction, Biomedical Imaging: Nano to Macro, 2004. IEEE International Symposium on, pp. 908-911 Vol. 1.

Bookstein, F.L., 1989. Principal warps: thin-plate splines and the decomposition of deformations. Pattern Analysis and Machine Intelligence, IEEE Transactions on, 11(6): 567-585.

Bredbenner, T.L. et al., 2010. Statistical shape modeling describes variation in tibia and femur surface geometry between Control and Incidence groups from the osteoarthritis initiative database. J Biomech, 43(9): 1780-6.

Brett, A.D., Taylor, C.J., 2000. A method of automated landmark generation for automated 3D PDM construction. Image and Vision Computing, 18(9): 739-748.

Browne, M., Langley, R.S., Gregson, P.J., 1999. Reliability theory for load bearing biomedical implants. Biomaterials, 20(14): 1285-92.

Brunon, A., Bruyere-Garnier, K., Coret, M., 2010. Mechanical characterization of liver capsule through uniaxial quasi-static tensile tests until failure. J Biomech, 43(11): 2221-7.

Chen, J.-H., Shapiro, L.G., 2009. 3D point correspondence by minimum description length with 2DPCA, Engineering in Medicine and Biology Society, 2009. EMBC 2009. Annual International Conference of the IEEE, pp. 5657-5660.

Chen, J.-H., Zheng, K.C., Shapiro, L.G., 2010. 3D point correspondence by minimum description length in feature space, Proceedings of the 11th European conference on computer vision conference on Computer vision: Part III. Springer-Verlag, Heraklion, Crete, Greece, pp. 621-634.

Cheynel, N. et al., 2011. Abdominal and pelvic injuries caused by road traffic accidents: characteristics and outcomes in a French cohort of 2,009 casualties. World J Surg, 35(7): 1621-5.

Chui, C., Kobayashi, E., Chen, X., Hisada, T., Sakuma, I., 2007. Transversely isotropic properties of porcine liver tissue: experiments and constitutive modelling. Med Biol Eng Comput, 45(1): 99-106.

Coleman, T., 2011. MATLAB Optimization Toolbox User's Guide. The MathWorks, Inc., Natick, MA.

Dalal, P. et al., 2007. A fast 3D correspondence method for statistical shape modeling, Computer Vision and Pattern Recognition, 2007. CVPR '07. IEEE Conference on, pp. 1-8.

Dar, F.H., Meakin, J.R., Aspden, R.M., 2002. Statistical methods in finite element analysis. J Biomech, 35(9): 1155-61.

Daruwalla, Z.J., Courtis, P., Fitzpatrick, C., Fitzpatrick, D., Mullett, H., 2010. Anatomic variation of the clavicle: a novel three-dimensional study. Clin Anat, 23(2): 199-209.

Davies, R.H., 2002. Learning shape: optimal models for analysing natural variability, University ofManchester.

Davies, R.H., Twining, C.J., Cootes, T.F., Taylor, C.J., 2010. Building 3-D statistical shape models by direct optimization. Medical Imaging, IEEE Transactions on, 29(4): 961-981.

DeWit, J.A., Cronin, D.S., 2012. Cervical spine segment finite element model for traumatic

injury prediction. J Mech Behav Biomed Mater, 10: 138-50.

Dryden, I.L., Mardia, K.V., 1998. Statistical shape analysis. John Wiley & Sons, Inc.

Elhagediab, A., Rouhana, S., 1998. Patterns of abdominal injury in frontal automotive crashes, 16th International Technical Conference on the Enhanced Safety of Vehicles, Windsor, Ontario, Canada.

Fink, W.L., Zelditch, M.L., 1997. Shape analysis and taxonomic status of Pygocentrus piranhas (Ostariophysi, Characiformes) from the Paraguay and Paraná river basins of South America. Copeia 1: 179-182.

Fitzgibbon, A.W., 2003. Robust registration of 2D and 3D point sets. Image and Vision Computing, 21(13–14): 1145-1153.

Fleute, M., Lavallée, S., Julliard, R., 1999. Incorporating a statistically based shape model into a system for computer-assisted anterior cruciate ligament surgery. Medical Image Analysis, 3(3): 209-222.

Fripp, J. et al., 2005. 3D Statistical shape models to embed spatial relationship information, Proceedings of the 1st International Workshop on Computer Vision for Biomedical Image Applications, pp. 51-60.

Gao, Z., Desai, J.P., 2010. Estimating zero-strain states of very soft tissue under gravity loading using digital image correlation. Medical Image Analysis, 14(2): 126-137.

Gao, Z., Lister, K., Desai, J.P., 2010. Constitutive modeling of liver tissue: experiment and theory. Ann Biomed Eng, 38(2): 505-16.

Geißler, G., Netzker, C., Kaliske, M., 2010. Discrete crack path prediction by an adaptive cohesive crack model. Engineering Fracture Mechanics, 77(18): 3541-3557.

Gokgol, C., Basdogan, C., Canadinc, D., 2012. Estimation of fracture toughness of liver tissue: Experiments and validation. Medical Engineering & Physics, 34(7): 882-891.

Gras, L.-L., Mitton, D., Viot, P., Laporte, S., 2012. Hyper-elastic properties of the human sternocleidomastoideus muscle in tension. Journal of the Mechanical Behavior of Biomedical Materials, 15(0): 131-140.

Greingor, J.L., Lazarus, S., 2006. Chest and abdominal injuries caused by seat belt wearing. South Med J, 99(5): 534-5.

Hallquist, J.O., 2007. LS-DYNA keyword user's manual, Livermore, California.

Hayes, A.R., Gayzik, F.S., Moreno, D.P., Martin, R.S., Stitzel, J., 2013a. Comparison of organ location, morphology, and rib coverage of a midsized male in the supine and seated positions. Comput Math Methods Med, 2013: 419821.

Hayes, A.R., Gayzik, F.S., Moreno, D.P., Martin, R.S., Stitzel, J.D., 2013b. Abdominal organ location, morphology, and rib coverage for the 5th, 50th, and 95th percentile males and females in the supine and seated posture using multi-modality imaging, Ann Avd Automot Med., Quebec City, Canada.

He, Q. et al., 2009. Detecting 3D corpus callosum abnormalities in phenylketonuria. Int J Comput Biol Drug Des, 2(4): 289-301.

He, Q., Duan, Y., Karsch, K., Miles, J., 2010. Detecting corpus callosum abnormalities in autism based on anatomical landmarks. Psychiatry Res, 183(2): 126-32.

Heimann, T., Meinzer, H.-P., 2009. Statistical shape models for 3D medical image segmentation: a review. Medical Image Analysis, 13(4): 543-563.

Hollenstein, M., Nava, A., Valtorta, D., Snedeker, J.G., Mazza, E., 2006. Mechanical characterization of the liver capsule and parenchyma. In: Harders, M., Székely, G. (Eds.), Biomedical Simulation. Lecture Notes in Computer Science. Springer Berlin Heidelberg, pp. 150-158.

Holzapfel, G.A., 2000. Nonlinear solid mechanics: a continuum approach for engineering. Wiley, Chichester, UK.

Howes, M.K., Gregory, T.S., Hardy, W.N., Beillas, P.D., 2012. Kinematics of the thoracoabdominal contents under various loading scenarios. Stapp car crash journal, 56: 1-48.

Hu, J. et al., 2009. Quantifying dynamic mechanical properties of human placenta tissue using optimization techniques with specimen-specific finite-element models. J Biomech, 42(15): 2528-34.

Hu, J. et al., 2011. A stochastic visco-hyperelastic model of human placenta tissue for finite element crash simulations. Ann Biomed Eng, 39(3): 1074-83.

Hufnagel, H., Pennec, X., Ehrhardt, J., Ayache, N., Handels, H., 2009. Computation of a probabilistic statistical shape model in a maximum-a-posteriori framework. Methods Inf Med, 48(4): 314-9.

Jin, W., Deng, L., Lv, H., Zhang, Q., Zhu, J., 2013. Mechanisms of blunt liver trauma patterns: An analysis of 53 cases. Exp Ther Med, 5(2): 395-398.

Kemper, A.R., Santago, A.C., Stitzel, J.D., Sparks, J.L., Duma, S., 2010. Biomechanical

response of human liver in tensile loading. Ann Adv Automot Med, 54: 15-26.

Kemper, A.R., Santago, A.C., Stitzel, J.D., Sparks, J.L., Duma, S., 2013. Effect of strain rate on the material properties of human liver parenchyma in unconfined compression. J Biomech Eng.

Kemper, A.R., Santago, A.C., Stitzel, J.D., Sparks, J.L., Duma, S.M., 2012. Biomechanical response of human spleen in tensile loading. J Biomech, 45(2): 348-55.

Kerdok, A.E., Ottensmeyer, M.P., Howe, R.D., 2006. Effects of perfusion on the viscoelastic characteristics of liver. Journal of Biomechanics, 39(12): 2221-2231.

Klatt, D. et al., 2010. Viscoelastic properties of liver measured by oscillatory rheometry and multifrequency magnetic resonance elastography. Biorheology, 47(2): 133-41.

Kolling, S., Bois, P.A.D., Benson, D.J., Feng, W.W., 2007. A tabulated formulation of hyperelasticity with rate effects and damage. Computational Mechanics, 40(5): 885-899.

Lafon, Y., Smith, F.W., Beillas, P., 2010. Combination of a model-deformation method and a positional MRI to quantify the effects of posture on the anatomical structures of the trunk. Journal of Biomechanics, 43(7): 1269-1278.

Lamecker, H., Lange, T., Seebass, M., 2002. A statistical shape model for the liver, Proceedings of the 5th International Conference on Medical Image Computing and Computer-Assisted Intervention-Part II pp. 421-427.

Lamecker, H., Wenckebach, T.H., Hege, H.C., 2006. Atlas-based 3D-shape reconstruction from X-ray images, Pattern Recognition, 2006. ICPR 2006. 18th International Conference on, pp. 371-374.

Lessley, D., Crandall, J.R., Shaw, G., Kent, R.W., Funk, J., 2004. A normalization technique for developing corridors from individual subject responses. SAE Technical Paper, 2004-01-0288.

Li, Z. et al., 2010. Rib fractures under anterior-posterior dynamic loads: experimental and finite-element study. J Biomech, 43(2): 228-34.

Lilliefors, H.W., 1967. On the Kolmogorov-Smirnov test for normality with mean and variance unknown. Journal of the American Statistical Association, 62(318): 399-402.

Liu, Z., Bilston, L., 2000. On the viscoelastic character of liver tissue: experiments and modelling of the linear behaviour. Biorheology, 37(3): 191-201.

Lorenz, C., Krahnstover, N., 1999. 3D statistical shape models for medical image segmentation, 3-D Digital Imaging and Modeling, 1999. Proceedings. Second International Conference on, pp. 414-423.

Lu, Y.-C., Untaroiu, C.D., 2013a. Effect of storage methods on indentation-based material properties of abdominal organs. Proceedings of the Institution of Mechanical Engineers, Part H: Journal of Engineering in Medicine, 227(3): 293-301.

Lu, Y.-C., Untaroiu, C.D., 2013b. Statistical shape analysis of clavicular cortical bone. Computer Methods and Programs in Biomedicine.

Mao, H. et al., 2013. Development of a Finite Element Human Head Model Validated With Forty Nine Loading Cases From Experimental and Real World Impacts. J Biomech Eng.

Marai, G.E., Grimm, C.M., Laidlaw, D.H., 2007. Arthrodial Joint Markerless Cross-Parameterization and Biomechanical Visualization. Visualization and Computer Graphics, IEEE Transactions on, 13(5): 1095-1104.

Mehrez, L., Bah, M.T., Browne, M., 2005. The application of probabilistic methods for assessment of hip replacement integrity, Transactions of the 51st Annual Meeting of the Orthopaedic Research Society, pp. 163.

Melis, M.E., Zaretsky, E.V., August, R., 1999. Probabilistic analysis of aircraft gas turbine disk life and reliability. J. Propul. Power, 15(5): 658–666.

Menk, A., Bordas, S.P.A., 2010. Numerically determined enrichment functions for the extended finite element method and applications to bi-material anisotropic fracture and polycrystals. International Journal for Numerical Methods in Engineering, 83(7): 805-828.

Nahum, A.M., Melvin, J.W., 2002. Accidental injury: biomechanics and prevention. Springer.

Ng, H.W., Teo, E.C., 2004. Probabilistic design analysis of the influence of material property on the human cervical spine. J Spinal Disord Tech, 17(2): 123-33.

Nicolella, D.P., Thacker, B.H., Katoozian, H., Davy, D., 2001. Probabilistic risk analysis of a cemented hip implant. ASME Bioeng. Div., 50: 427–428.

Nicolella, D.P., Thacker, B.H., Katoozian, H., Davy, D.T., 2006. The effect of three-dimensional

shape optimization on the probabilistic response of a cemented femoral hip prosthesis. J Biomech, 39(7): 1265-78.

Nicolle, S., Vezin, P., Palierne, J.F., 2010. A strain-hardening bi-power law for the nonlinear behaviour of biological soft tissues. J Biomech, 43(5): 927-32.

Ocal, S., Ozcan, M.U., Basdogan, I., Basdogan, C., 2010. Effect of preservation period on the viscoelastic material properties of soft tissues with implications for liver transplantation. J Biomech Eng, 132(10): 101007.

Ogden, R.W., 1997. Non-linear elastic deformations. Dover Publications, Mineola, NY.

Okada, T. et al., 2007. Automated Segmentation of the Liver from 3D CT Images Using Probabilistic Atlas and Multi-level Statistical Shape Model. In: Ayache, N., Ourselin, S., Maeder, A. (Eds.), Medical Image Computing and Computer-Assisted Intervention – MICCAI 2007. Lecture Notes in Computer Science. Springer Berlin Heidelberg, pp. 86-93.

Oniscu, G.C., Parks, R.W., Garden, O.J., 2006. Classification of liver and pancreatic trauma. HPB (Oxford), 8(1): 4-9.

Ottensmeyer, M.P., 2001. Minimally invasive instrument for in vivo measurement of solid organ mechanical impedance, Massachusetts Institute of Technology, Cambridge, MA.

Palmberg, B., Blom, A.F., Eggwertz, S., 1987. Probabilistic damage tolerance analysis of aircraft structures. In: Provan, J. (Ed.), Probabilistic fracture mechanics and reliability. Engineering Application of Fracture Mechanics. Springer Netherlands, pp. 47-130.

Pannachet, T., Sluys, L.J., Askes, H., 2009. Error estimation and adaptivity for discontinuous failure. International Journal for Numerical Methods in Engineering, 78(5): 528-563.

Pervin, F., Chen, W.W., Weerasooriya, T., 2011. Dynamic compressive response of bovine liver tissues. J Mech Behav Biomed Mater, 4(1): 76-84.

Rajamani, K.T. et al., 2007. Statistical deformable bone models for robust 3D surface extrapolation from sparse data. Med Image Anal, 11(2): 99-109.

Reed, M.P., Sochor, M.M., Rupp, J.D., Klinich, K.D., Manary, M.A., 2009. Anthropometric specification of child crash dummy pelves through statistical analysis of skeletal geometry. Journal of Biomechanics, 42(8): 1143-1145.

Reyes, M., González Ballester, M.A., Kozic, N., Summers, R.M., Linguraru, M.G., 2010. Hierarchical patch generation for multilevel statistical shape analysis by principal factor analysis decomposition. 762617-762617.

Roan, E., Vemaganti, K., 2007. The nonlinear material properties of liver tissue determined from no-slip uniaxial compression experiments. J Biomech Eng, 129(3): 450-6.

Rosen, J., Brown, J.D., De, S., Sinanan, M., Hannaford, B., 2008. Biomechanical properties of abdominal organs in vivo and postmortem under compression loads. J Biomech Eng, 130(2): 021020.

Samur, E., Sedef, M., Basdogan, C., Avtan, L., Duzgun, O., 2007. A robotic indenter for minimally invasive measurement and characterization of soft tissue response. Med Image Anal, 11(4): 361-73.

Santago, A.C., Kemper, A.R., McNally, C., Sparks, J.L., Duma, S., 2009a. Freezing affects the mechanical properties of bovine liver. Biomed Sci Instrum, 45: 24-9.

Santago, A.C., Kemper, A.R., McNally, C., Sparks, J.L., Duma, S.M., 2009b. The effect of temperature on the mechanical properties of bovine liver. Biomed Sci Instrum, 45: 376-81.

Shin, J., Untaroiu, C., 2013. Biomechanical and Injury Response of Human Foot and Ankle under Complex Loading. J Biomech Eng.

Shin, J., Yue, N., Untaroiu, C.D., 2012. A finite element model of the foot and ankle for automotive impact applications. Ann Biomed Eng, 40(12): 2519-31.

Styner, M.A. et al., 2003. Evaluation of 3D correspondence methods for model building. Information processing in medical imaging : proceedings of the ... conference, 18: 63-75.

Tallarida, R.J., Murray, R.B., 1986. Mann-Whitney Test, Manual of Pharmacologic Calculations. Springer New York, pp. 149-153.

Tamura, A. et al., 2002. Mechanical characterization of porcine abdominal organs. Stapp Car Crash J, 46: 55-69.

Uehara, H., 1995. A study on the mechanical properties of the kidney, liver, and spleen, by means of tensile stress test with variable strain velocity. Journal of Kyoto Prefectural University of Medicine, 104(1): 439-451.

Umale, S. et al., 2013. Experimental mechanical characterization of abdominal organs: liver, kidney & spleen. J Mech Behav Biomed Mater, 17: 22-33.

Umut Ozcan, M., Ocal, S., Basdogan, C., Dogusoy, G., Tokat, Y., 2011. Characterization of frequency-dependent material properties of human liver and its pathologies using an impact hammer. Med Image Anal, 15(1): 45-52.

Untaroiu, C.D., 2005. Development and Validation of a Finite Element Model of Human Lower Limb: Including Detailed Geometry, Physical Material Properties, and Component Validations for Pedestrian Injuries, University of Virginia.

Untaroiu, C.D., 2010. A numerical investigation of mid-femoral injury tolerance in axial compression and bending loading. Int. J. Crashworthiness 15(1): 83-92.

Untaroiu, C.D., 2013. The influence of the specimen shape and loading conditions on the parameter identification of a viscoelastic brain model. Comput Math Methods Med, 2013: 460413.

Untaroiu, C.D., Adam, T.J., 2013. Performance-Based Classification of Occupant Posture to Reduce the Risk of Injury in a Collision. Intelligent Transportation Systems, IEEE Transactions on, 14(2): 565-573.

Untaroiu, C.D. et al., 2012. Effect of seat belt pretensioners on human abdomen and thorax: biomechanical response and risk of injuries. J Trauma Acute Care Surg, 72(5): 1304-15.

Untaroiu, C.D., Darvish, K., Crandall, J., Deng, B., Wang, J.T., 2005. A finite element model of the lower limb for simulating pedestrian impacts. Stapp Car Crash J, 49: 157-81.

Untaroiu, C.D., Lu, Y.-C., 2013. Material characterization of liver parenchyma using specimen-specific finite element models. Journal of the Mechanical Behavior of Biomedical Materials, 26: 11-22.

Untaroiu, C.D. et al., 2008. A study of the pedestrian impact kinematics using finite element dummy models: the corridors and dimensional analysis scaling of upper-body trajectories. International Journal of Crashworthiness, 13(5): 469-478.

Untaroiu, C.D., Yue, N., Shin, J., 2013. A finite element model of the lower limb for simulating automotive impacts. Ann Biomed Eng, 41(3): 513-26.

Valtorta, D., Mazza, E., 2005. Dynamic measurement of soft tissue viscoelastic properties with a torsional resonator device. Med Image Anal, 9(5): 481-90.

van de Giessen, M. et al., 2010. Statistical descriptions of scaphoid and lunate bone shapes. J Biomech, 43(8): 1463-9.

van de Giessen, M. et al., 2009. A statistical description of the articulating ulna surface for prosthesis design, Biomedical Imaging: From Nano to Macro, 2009. ISBI '09. IEEE International Symposium on, pp. 678-681.

Vavalle, N., Moreno, D., Rhyne, A., Stitzel, J., Gayzik, F.S., 2013. Lateral Impact Validation of a Geometrically Accurate Full Body Finite Element Model for Blunt Injury Prediction. Annals of Biomedical Engineering, 41(3): 497-512.

Vezin, P., Verriest, J.P., 2005. Development of a set of numerical human models for safety, Proceedings of the 19th International Technical Conference on the Enhanced Safety of Vehicles.

Volokh, K.Y., 2010. On modeling failure of rubber-like materials. Mechanics Research Communications, 37(8): 684-689.

Xi, P., Lee, W.-S., Shu, C., 2007. Analysis of segmented human body scans, Proceedings of Graphics Interface 2007. ACM, Montreal, Canada, pp. 19-26.

Yamada, H., 1970. Strength of biological materials. Williams and Wilkins, Huntingdon, NY.

Yeh, W.-C. et al., 2002. Elastic modulus measurements of human liver and correlation with pathology. Ultrasound in Medicine & Biology, 28(4): 467-474.

Zhang, Y., Liu, Q., 2002. Reliability-based design of automobile components. Proc. Inst. Mech. Eng. Part D: J. Automob. Eng., 216(6): 455–471.

Zhang, Z.Y., 1992. On Local Matching of Free-Form Curves, pp. 345-356.

Zheng, G. et al., 2009. A 2D/3D correspondence building method for reconstruction of a patient-specific 3D bone surface model using point distribution models and calibrated X-ray images. Med Image Anal, 13(6): 883-99.